



# Visible-light-mediated remote aliphatic C—H oxyfunctionalization over CuCl<sub>2</sub> decorated hollowed-TS-1 photocatalysts

Hui Yin<sup>a</sup>, Feng Su<sup>a</sup>, Chao Luo<sup>a</sup>, Lixia Zhu<sup>a</sup>, Wenzhou Zhong<sup>a,\*</sup>, Liqiu Mao<sup>a,\*</sup>, Kuiyi You<sup>b</sup>, Dulin Yin<sup>a</sup>

<sup>a</sup> National & Local United Engineering Laboratory for New Petrochemical Materials & Fine Utilization of Resources, Key Laboratory of Chemical Biology Traditional Chinese Medicine Research Ministry of Education, College of Chemistry and Chemical Engineering, Hunan Normal University, Changsha 410081, China

<sup>b</sup> College of Chemical Engineering, Xiangtan University, Xiangtan 411105, China

## ARTICLE INFO

### Keywords:

Hollow TS-1 zeolite  
Oxyfunctionalization  
Alkane  
Photocatalysis

## ABSTRACT

Selective oxygenation of alkanes via C—H bond activation still remains a challenge because the oxygen-containing products are more active than the substrates. Here, we develop a new concept of eco-friendly zeolite-fixed photocatalyst to impart catalytic performance via loading CuCl<sub>2</sub> upon visible-light irradiation. Complete selectivity in terms of the final oxidation product KA-oil was obtained with 24% conversion in the application of cyclohexane oxidation. After optimization, the desired ketones and alcohols were also obtained in good to excellent selectivities with broad substrate scope. Multiple experimental studies combined with theoretical calculations demonstrate that the formation of the unique CuCl<sub>2</sub>/TS-1 hollow structure with isolated CuCl<sub>2</sub> species anchored onto the inner and outer surface of TS-1 shells: the function of the major tetrahedral Ti—O<sub>4</sub> sites in heterojunctions to isolate energy levels near the conduction and valence bands. In photocatalysis, the presence of Cu—O—Ti—O<sub>3</sub> heterojunctions facilitates separation and transfer of photogenerated electrons and holes

## 1. Introduction

Selective partial oxidation of alkanes by O<sub>2</sub> is one of the most important processes for the manufacture of fine chemicals and industrial intermediates in chemical industry. Hereinto, the industrial oxidation of cyclohexane by O<sub>2</sub> is an important reaction for the production of KA-oils (a mixture of cyclohexanol and cyclohexanone), which are the intermediates to synthesize caprolactam and nylons [1,2]. Despite tremendous potential, the low reactivity of C—H bonds coupled with the difficulty of achieving high selectivity in the use of molecular oxygen pose significant challenge for the realization of a C—H oxyfunctionalization strategy, especially for more inert feature of aliphatic C—H bonds. The reason is that for such conventional thermodynamic driving catalysis with high temperature, autoxidations as radical chain processes are inherently unselective [3,4], in which molecular oxygen attacks partially oxidized products more easily than the starting hydrocarbon under thermal conditions. Furthermore, unrestricted mobility of the free radical intermediates results in indiscriminate attack

on starting alkane and primary oxidation products. Therefore, the KA-oil selectivity of commercial cyclohexane oxidation reactions under practical conditions (high pressure and high temperature) is limited to 70% at < 7% conversion. Currently, the main problem that prevents selective synthesis at higher cyclohexane conversion is still the KA-oil over-oxidation and environmental problem-massive discharges of waste [5]. Over the past decade, aerobic oxyfunctionalization of aliphatic C—H oxidation has been investigated using transition metal catalysts (Ru, Fe, V, Co, Mn or Ir) and organocatalysts [1,6], allowing a lower temperature-driven catalytic reaction. Despite the great strides in aliphatic C—H oxidation, the ability to control the chemistry of the mildly produced radicals and unrestricted mobility of the free radical intermediates in indiscriminate attack on primary oxidation products remains an unsolved problem under thermal catalytic processes.

The development of an effective route for C—H functionalization using molecular oxygen as the oxidant under mild conditions is highly desirable [7–9]. Recently, photocatalysis could provide an alternative and green approach to drive the selective oxygenation of alkane to

\* Corresponding authors at: National & Local United Engineering Laboratory for New Petrochemical Materials & Fine Utilization of Resources, Key Laboratory of Chemical Biology Traditional Chinese Medicine Research Ministry of Education, College of Chemistry and Chemical Engineering, Hunan Normal University, Changsha 410081, China.

E-mail addresses: [zwenz79@163.com](mailto:zwenz79@163.com) (W. Zhong), [mlq1010@126.com](mailto:mlq1010@126.com) (L. Mao).

<https://doi.org/10.1016/j.apcatb.2021.120851>

Received 14 August 2021; Received in revised form 20 October 2021; Accepted 24 October 2021

Available online 30 October 2021

0926-3373/© 2021 Elsevier B.V. All rights reserved.

thermodynamically unstable alcohol and carbonyl products. Various photocatalytic systems based on transition-metal oxides, bismuth-containing semiconductors, cadmium sulfide,  $g\text{-C}_3\text{N}_4$  and hybrid-composites have been developed for such applications [10–14]. Among them, heterogeneous  $\text{TiO}_2$  photocatalysts are extensively studied in alkane photoredox process [15–18]. Nevertheless, the efficiency for photocatalytic alkane oxidation on  $\text{TiO}_2$  is very low due to the high positive energy of the photogenerated holes. To enhance the photocatalytic efficiency on  $\text{TiO}_2$ , two innovative methods were proposed for a decrease of optical band gap energy. One case is doping  $\text{TiO}_2$  with transition metals and nonmetal atom, another case is anchoring a dye-sensitizer molecule on the surface [5,19–21]. It's also worth noting that  $\text{TiO}_2$  nanoparticles that anchored onto supports show a much higher photocatalytic selectivity than the bulk  $\text{TiO}_2$ , indicating that these alkane photoreactions depend strongly on the photocatalyst structures.

Titanium silicalite-1 (TS-1) with MFI cages connected by 10-ring pore openings, where highly dispersed  $\text{Ti}^{4+}$  exists in a tetrahedral coordination environment ( $\text{Ti}-\text{O}_4$  units), has been known for its remarkable thermal catalytic activity for the C–H bond of hydrocarbons in the chemical industry [22–24]. These isolated  $\text{Ti}-\text{O}_4$  units in the silicate framework, therefore, lack a bulk semiconducting character and show photocatalytic activity quite different from that of bulk crystalline  $\text{TiO}_2$  (which consists of octahedrally coordinated  $\text{Ti}-\text{O}_6$  units). The unique local  $\text{Ti}-\text{O}_4$  units distributed in the framework favour the single electron transfer from the adjacent lattice oxygen to metal atom under light excitation, resulting in a higher photocatalytic activity. As a matter of fact, some photocatalytic processes involving the transformation of substrates on  $\text{Ti}-\text{O}_4$  units is highly selective: for example,  $\text{CO}_2$  photo-reduction [25], benzyl alcohol photooxidation [26] and water splitting [27]. However, the true chemical nature and reactivities of these  $\text{Ti}-\text{O}_4$  units as a photocatalyst are yet little known, especially the photocatalytic reactivity for the C–H bond of alkane by  $\text{O}_2$ . On the other hand, the zeolite-based photocatalysts have been developed, where the porous systems of the zeolites were employed to stabilize the active sites or provide the shape selectivity for the multiple reactants. Wang and co-workers reported that the N-oxyl radicals trapped on zeolite surface can accelerate photocatalysis [28]. Frei et al. used large-pore alkali or alkaline-earth zeolites to achieve the partial oxidation of olefins with unprecedented selectivity using visible light [29]. Yet, some disadvantages of porous zeolites in the photocatalysis still need for further exploration, particularly, the diffusion and transport of large molecules would be greatly limited by the microporous channels (0.51 nm), resulting in a low photocatalytic activity.

Recently, the ability of  $\text{CuCl}_2$  to function as visible-light photocatalyst has been recognized, leading to exciting new possibilities for unprecedented aliphatic C–H oxidation. Takaki and co-workers reported that a visible-light radiation could promote  $\text{CuCl}_2$  homolysis, then worked with a variety of alkane substrates to deliver corresponding alcohols and ketones (<70% selectivity) [30]. To improve the photocatalytic efficiency of  $\text{CuCl}_2$ , the co-feeding of concentrated HCl as the chlorine radicals for the C–H bond activation of cyclohexane has been revealed [31], but oxy-chlorination of cyclohexane easily occurs to chlorinated byproducts. In addition to  $\text{CuCl}_2$ -based photocatalysts,  $\text{FeCl}_3$  and  $\text{VOCl}_3$  with easily changeable valence have also been found to be active for the aerobic oxidation of alkanes into alcohols and ketones under mild conditions, but affording a higher chlorocyclohexane or cyclohexene selectivity [30–32]. Reported examples indicate that an appealing strategy involving visible light-accelerated homolysis of the M–Cl bonds by a charge-transfer ligand-to-metal (CTLM) excited state has been developed to give extremely reactive chlorine radicals, which abstract hydrogen atoms from the C–H bonds of alkanes for the catalytic cycle. For comparison, other metal chlorides containing metal cations of low oxidizability, such as  $\text{ZnCl}_2$ ,  $\text{TiCl}_4$ ,  $\text{CoCl}_2$ ,  $\text{MnCl}_2$ ,  $\text{SnCl}_4$ ,  $\text{CaCl}_2$  and  $\text{NiCl}_2$ , had hardly any response to the visible light of this region, as a consequence of their  $\text{M}^{n+}\text{Cl}^- \rightarrow \text{M}^{(n-1)+}\text{Cl}$  transition needing a higher

energy [33]. Therefore, low cost and readily available  $\text{CuCl}_2$  have good photocatalytic efficiency in the case of adding concentrated HCl, but photo-assisted oxy-chlorination of cyclohexane easily occurs and the selectivity of alcohols and ketones in the reaction products remains a big challenge to be improved. Finding a highly efficient  $\text{CuCl}_2$ -based catalytic system without the corrosive additives has been desired in view of green chemistry.

From the above results it is clear that, TS-1 zeolite has the advantage (as commented above) of being a selective photocatalyst. However, efficient photocatalysts further need to strengthen the processes of radical formation for the alkane oxidation: (1) absorb visible-light across the UV-light region to form electrons and holes; (2) enhance the charge carrier separation between the electrons and holes in space to prevent their recombination; (3) have a suitable redox potential to drive the photo-oxidative reaction; (4) possess the mass transport ability of a guest molecule to internal catalytic sites. In this work, a kind of hollow-structured TS-1 (HTS-1) prepared via the simple recrystallization of solid-structured TS-1 to one-step fabricate the large zeolite cage and the Ti species anchored onto zeolite. One considers that the large zeolite cages favor the diffusion of the bulky molecules to internal catalytic sites, whereas in the other rich Ti species are believed to be effective traps for the photoformed holes, thus reducing their recombination with the electrons. Then, the  $\text{CuCl}_2$  species were loaded onto the HTS-1 zeolite with heterojunction interface in which the photogenerated holes oxidize the Cu–Cl bond of  $\text{CuCl}_2$  into chlorine radicals and further to initiate the C–H activation of alkane through a radical pathway under visible light irradiation.

## 2. Experimental

### 2.1. Catalyst preparation

TS-1 zeolites was synthesized by hydrothermal treatment of an aqueous gel containing tetraethyl orthosilicate (TEOS), titanium butoxide (TBOT), alkali-free tetrapropyl ammonium hydroxide (TPAOH) and anhydrous isopropanol. The starting gel with the chemical composition  $\text{SiO}_2$ : 0.4TPAOH: 0.01 $\text{TiO}_2$ : 40  $\text{H}_2\text{O}$ , was transferred to a Teflon-lined stainless steel autoclave, and hydrothermal heating treatment was performed at 170 °C for 3 days in an air oven. The solid product obtained was separated by centrifugation, washed with distilled water, dried at 120 °C overnight, and finally calcined at 500 °C for 10 h. The hollow TS-1 (HTS-1) was synthesized by the dissolution-recrystallization process [5,22], and previously calcined TS-1 was treated with  $\text{H}_2\text{SO}_4$  solution (TS-1:  $\text{H}_2\text{SO}_4$ :  $\text{H}_2\text{O}$  = 10: 1.0: 140) for 3 h at room temperature. The acid-treated TS-1 was dispersed in TPAOH solution (10 TS-1: 1.5 TPAOH:125  $\text{H}_2\text{O}$ ), and was recrystallized at 140 °C for 3 days. The solid was isolated, washed, dried and finally calcined at 500 °C for 10 h. The hollow-structured TS-1 with low Ti content (LTS-1) and the hollow-structured silicalite-1 without adding titanium were also prepared under an identical procedure.

The  $\text{CuCl}_2$ -modified zeolites was synthesized by means of incipient wetness impregnation of HTS-1 with an EtOH and  $\text{H}_2\text{O}$  (1:1) solution of  $\text{CuCl}_2$  to give 10 wt% of  $\text{CuCl}_2$  in the final samples. The volumes of the solution used were sufficient to completely wet the HTS-1 supports. The impregnated samples were slowly allowed to evaporate at 60 °C vacuum drying till dryness under vigorous stirring conditions. The investigated samples were denoted as x  $\text{CuCl}_2$ /HTS, where x is the  $\text{CuCl}_2$  content in support of the weight percentage. For comparison,  $\text{CuCl}_2$ /TS-1,  $\text{CuCl}_2$ /LTS-1,  $\text{CuCl}_2$ /P25 and  $\text{CuCl}_2$ /Silicalite-1 were also synthesized using the same procedure.

### 2.2. Catalyst characterization

X-ray powder diffraction (XRD) patterns were recorded by a Bruker D8 Advance XRD using  $\text{CuK}\alpha$  radiation ( $\lambda = 1.542 \text{ \AA}$ ). Transmission electron microscopy (TEM) and high-resolution TEM (HRTEM) images

were collected by a JEM-2100 microscope with an acceleration voltage of 200 kV. X-ray photoelectron spectroscopic (XPS) results (Cu 3d, Ti 2p and Cl 2p) of surface Cu, Ti and Cl species were collected over an Imaging Photoelectron Spectrometer (Axis Ultra, Kratos Analytical Ltd.) with Al K $\alpha$  radiation (1486.7 eV), and fit XPS software was used for curve fitting. Raman spectroscopy was obtained using a Renishaw in Via Raman Microscope system with a laser light of 514.5 nm. UV-vis spectra were detected by a Varian-Cary 5000 spectrometer using BaSO<sub>4</sub> background as reference. Brunauer-Emmett-Teller (BET) surface area and porosity were determined by N<sub>2</sub> adsorption-desorption isotherm measurements at 77 K over a Micromeritics Tristar-3000 nitrogen adsorption apparatus. Fourier transform infrared (FT-IR) spectra of KBr pellets were obtained on an AVATAR 370 Thermo Nicolet spectrophotometer with a resolution of 2 cm<sup>-1</sup>. Photoluminescence (PL) spectra were obtained by a JASCO FP-6500 type fluorescence spectrophotometer with an excitation wavelength of 290 nm light. TPR determinations were carried out in a temperature-programmed reduction system. The amount of catalyst (0.04 g) was held in place by glass wool plugs. Then, the gas mixture used was 5% H<sub>2</sub> in Ar at a flow-rate of 20 cm<sup>3</sup>/min, and the heating rate was 6 K/min. The analysis was carried out by use of an on-line gas chromatograph with conductivity detectors. The photocurrent response results were obtained on a CHI660B electrochemical workstation (Chenhua Instrument, Shanghai, China) using a standard three-electrode system: a FTO glass coated with a catalyst as working electrode, a platinum wire as counter electrode, and a standard calomel electrode in saturated KCl as reference electrode. EPR spectra were measured in 50  $\mu$ L quartz tubes on a Bruker A300-10/12/S at room temperature. EPR spectra were simulated using an extended version of the program Bruker WinEPR.

### 2.3. Density Functional Theory (DFT) calculation

DFT calculations were performed with the DMol3 code in Materials Studio of Accelrys Inc. on personal computers [34]. The generalized gradient approximation (GGA) with Perdew-Burke-Ernzerhof (PBE) functional is employed as the exchange-correlation functional [35]. The calculations used the double-numeric quality basis set with polarization functions (DNP), which is more accurate than a Gaussian basis set of 6-31 G\*. To improve computational performance, a Fermi smearing of 0.005 Ha and an orbital cutoff distance of 4.4 Å were set. The tolerances of the energy, gradient, and displacement convergences were  $2 \times 10^{-5}$  Ha,  $4 \times 10^{-3}$  Ha/Å, and  $5 \times 10^{-3}$  Å, respectively. The HTS-1 structure was modeled with a 48-T cluster (Si<sub>48</sub>O<sub>96</sub>H<sub>56</sub>), which was generated from two adjacent MFI unit cells ( $96 \times 2 = 192$  Si atoms and  $192 \times 2 = 384$  O atoms) with the initial lattice constants of  $a = 2.0022$  nm,  $b = 1.9899$  nm and  $c = 1.3383$  nm. The dangling bonds of the boundary O atoms in the cluster were saturated by H atoms. In order to minimize cluster boundary effects and better simulate the overall zeolite structure, the coordinates of these terminal OH groups were constrained. The terminal O atoms were constrained at their original positions in the MFI unit cell. In addition, some additional calculations including the role of dispersion forces were performed using the DFT-D for CuCl<sub>2</sub> decorated HTS-1, which have been shown to have a very significant effect on the interactions of CuCl<sub>2</sub> species [36]. Except for the terminal OH groups, all other atoms were optimized with CuCl<sub>2</sub> species.

### 2.4. Catalyst performance

Photocatalytic oxidation reactions using O<sub>2</sub> as oxidant were carried out under photoirradiation from a 300 W Xe lamp (PLS-SXE 300 C, Perfectlight, 2000 mW cm<sup>-2</sup>) with a 400 nm cut off filter in a closed stainless steel container equipped with a 50 mL Pyrex glass vessel (inner diameter 4 cm, inner height 7 cm) and an O-ring sealed quartz window covered the top to transmit light irradiation. The container was placed 8 cm away from the light source, and a water cooling system at interlayer keep the reaction temperature at 30 °C. Typically, cyclohexane (1 mmol)

and 50 mg of photocatalyst were mechanically mixed with 12 mL of acetonitrile in reactor. After being filled with the desired amount of oxygen (1.0 MPa), the reaction solution was irradiated under magnetically stirring. After the reaction, the catalyst particles were completely removed by centrifugation, and the products were analyzed using a SHIMADZU Gas Chromatograph (GC-2010, 30 m  $\times$  0.32 mm  $\times$  0.50  $\mu$ m DB-17 polysiloxane capillary column) equipped with FID detector using chlorobenzene as the internal standard. Both the injector and detector temperature were 250 °C, and the column temperature was 80 °C. The gas products were analyzed by gas chromatography (9790PLUS, Fuli Instruments, Zhejiang, China) equipped with a TCD detector. All products were satisfactorily identified by comparing the MS spectra with those of the authentic samples. The conversion of cyclohexane and selectivity of products were calculated using the formulas (Scheme S1). All raw materials and products were established carbon mass balances. All the experiments were repeated at least 3 times in parallel to obtain an average value.

## 3. Results and discussion

### 3.1. Photocatalyst properties

The crystallinity and morphology of the asprepared zeolite photocatalysts were observed by transmission electron microscopy (TEM). From Fig. 1, the pure HTS-1 zeolites exhibit clearly large intracrystalline voids, having an average particle size of 150–250 nm. The obvious contrast between the dark edge and the relatively bright center confirms their hollow nature. This unique large void morphology of our as-prepared HTS-1 zeolite by a dissolution-recrystallization process is located exclusively in the inner part of the crystals, which is distinctly different from that of normal solid TS-1 [37]. Meanwhile, unlike the smooth surface of the normal solid TS-1, a relatively rough surface emerges on the HTS-1 crystal. After loading with CuCl<sub>2</sub> species, TEM images show a similar hollow sphere-like structure and the formed CuCl<sub>2</sub> species are well dispersed on zeolite surface. The presence of intracrystalline voids accessible only via entrances smaller than 4 nm have been evidenced from abrupt closure at  $p/p_0 = 0.43$  on the desorption branch (Fig. 2A and B). It can also be seen that both the BET surface areas and pore diameter of CuCl<sub>2</sub>-modified zeolites are slightly lower than that of the pristine HTS-1 zeolite, which may be due to the pores of zeolite partly blocking by CuCl<sub>2</sub> species (Table S1). The XRD patterns of the as-prepared zeolite photocatalysts are shown in Fig. 2C. The characteristic MFI diffraction peaks for the pristine HTS-1 zeolite are present at 23.2° and 24.1°, and the diffraction peaks of the crystalline TiO<sub>2</sub> phase were not observed in the XRD patterns, indicating that the Ti species did not condense to form bulk TiO<sub>2</sub> oxides by a dissolution-recrystallization process. These Ti species were still highly incorporated into the MFI framework or homogeneously dispersed on the zeolite surface, as evidenced by TEM images. The introduction of CuCl<sub>2</sub> species results in a lower intensity for the more broad MFI-type diffraction peaks, which is attributed to the existence of strong interactions between CuCl<sub>2</sub> species and HTS-1 supports (the similar phenomenon is observed in the previous literatures [38]). With the increase of CuCl<sub>2</sub> species to 15 wt%, some small diffraction peaks at 22°, 34° and 41° attributable to CuCl<sub>2</sub> (JCPDS no. 33-0451) could be distinguished from the characteristic diffractions of HTS-1 [39], indicating heterogeneous dispersion of CuCl<sub>2</sub> as small cluster particle over the pore surface of HTS-1. Unlike bulk samples, the pores and large specific surface area of HTS-1 photocatalysts not only are beneficial for light scattering and absorption, but also facilitates reactant/product transfer for oxidation reactions. Additionally, this kind of hollow nature is also easy migration of photogenerated charges to the surfaces of HTS-1 zeolite because of the relatively thin shells.

The structure of the asprepared zeolite photocatalysts is characterized by Raman technique, which is sensitive to the chemical state of Ti species of these hollow TS-based samples. As shown in Fig. 3A, the

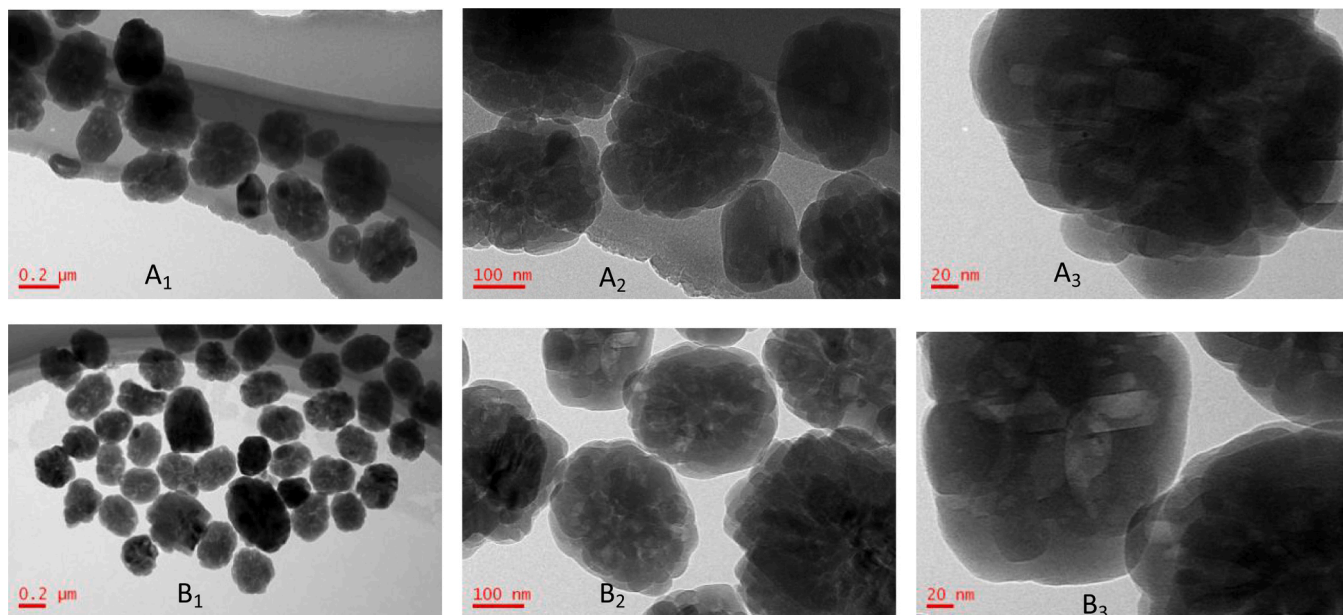


Fig. 1. TEM images of HTS-1 sample (A<sub>1</sub>, A<sub>2</sub> and A<sub>3</sub>) and 10 wt% CuCl<sub>2</sub>/HTS-1 sample (B<sub>1</sub>, B<sub>2</sub> and B<sub>3</sub>).

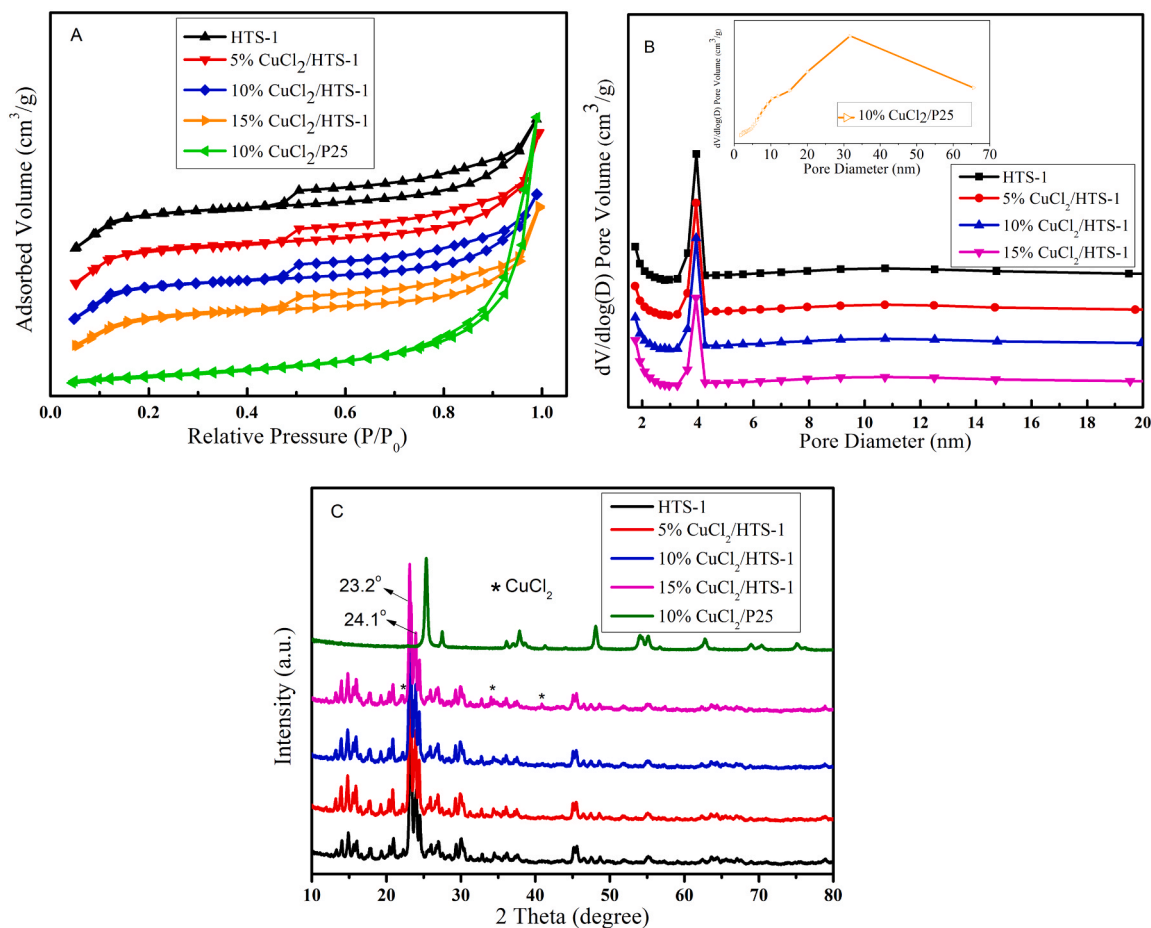


Fig. 2. N<sub>2</sub> adsorption-desorption isotherms (A) and pore diameter distribution (B) of different catalyst, XRD patterns of different samples (C).

pristine HTS-1 zeolite gives a weak Raman band at 554 cm<sup>-1</sup>, corresponding to the stretching modes of the framework Ti–O–Si bridges in the local Ti–O<sub>4</sub> unit [40]. Meanwhile, the characteristic bands of the extraframework Ti–O–Ti bridges appear at 389, 514 and 639 cm<sup>-1</sup>,

being an indicative of the existence of a handful of TiO<sub>2</sub> nanoparticles in the HTS-1 material [41]. After CuCl<sub>2</sub> species loading, these bands of modified HTS-1 decreases in intensity and its maximum shifts toward higher frequency, suggesting that the length and the coordination of the

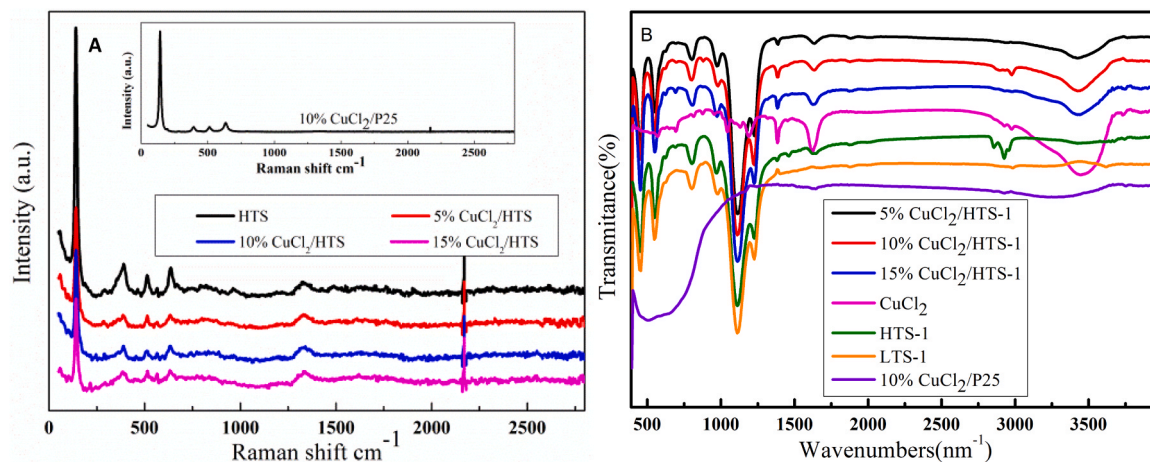


Fig. 3. UV-Raman spectra (A) and FT-IR spectra (B) of samples.

titanate wires (Ti–O–Si or Ti–O–Ti) varied significantly. Thus, oxygen vacancies are prone to form on CuCl<sub>2</sub>-modified HTS-1. With introduction of more CuCl<sub>2</sub> species, the new Raman band at 208 cm<sup>-1</sup>, which appears for 15 wt% CuCl<sub>2</sub>/HTS-1, are absent in the Raman spectra of HTS-1 and 10 wt% CuCl<sub>2</sub>/HTS-1. These new bands corresponding to Cu–Cl stretching and bending may be from the CuCl<sub>2</sub> clusters in CuCl<sub>2</sub>/HTS-1 [42], as shown in UV–vis DRS absorption with a narrowing

of the HOMO–LUMO gap. As shown in the infrared spectra (Fig. 3B), the enhanced intensity of the characteristic band at 950 cm<sup>-1</sup> for the HTS-1 zeolite with comparison of the silicate-1 without titanium species (Fig. S1) [43], further confirms the presence of the Ti–O<sub>4</sub> unit on the HTS-based catalysts. However, the position of this band shifts to a lower wavelength after the introduction of CuCl<sub>2</sub> species, confirming that the coordination of CuCl<sub>2</sub> species to a surface Ti–O<sub>4</sub> unit occurs. In addition,

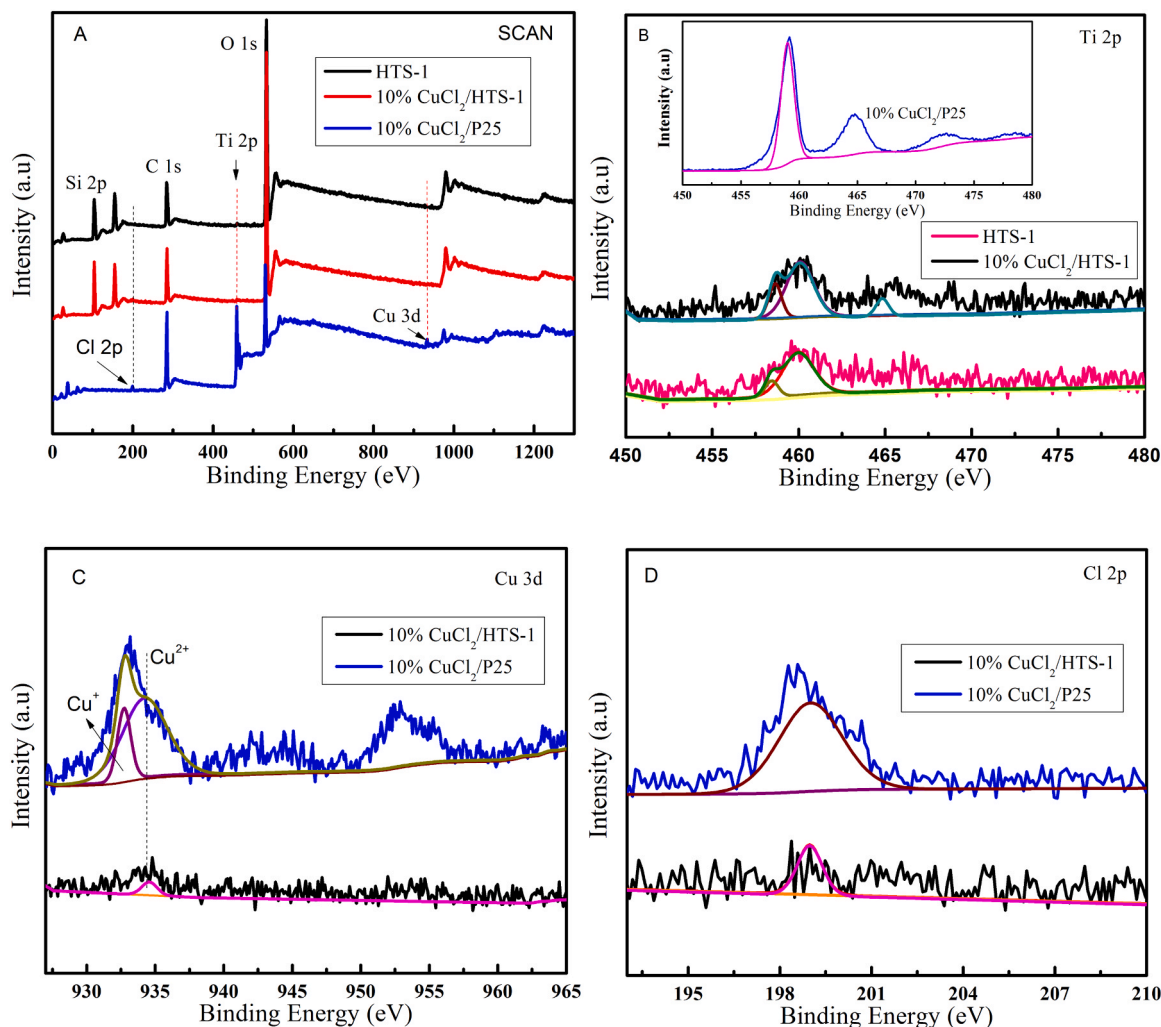


Fig. 4. XPS spectra of (A) survey, (B) Ti 2p, (C) Cu 3d and (D) Cl 2p.

the  $\text{CuCl}_2$ -modified HTS-1 samples have additional absorptions that are attributed to the stretching vibration of Cu–Cl groups; meanwhile, a band with the enhanced intensity attributed to the surface O–H groups can be observed at  $3743\text{ cm}^{-1}$ . The above results indicate that the bridge bonds of Ti–O–Si or Ti–O–Ti in the HTS-1 surface would be partially disrupted by  $\text{CuCl}_2$ , yielding numerous [O–Ti–O–Cu–Cl] sites exposed at the crystalline surfaces with a low rate of electron-hole pair recombination to facilitate the carrier separation.

Surface composition of the samples was further investigated using X-ray photoelectron spectroscopy (XPS). The XPS survey spectra of the asprepared photocatalysts indicate the presence of O, Ti, Cl and Cu elements (Fig. 4A). In the Ti 2p spectrum, the pristine sample of HTS-1 possessed the binding energy levels of Ti 2p<sub>3/2</sub> and Ti 2p<sub>1/2</sub> at around 459 eV and 464 eV, respectively (Fig. 4B). In contrast, the curves for  $\text{CuCl}_2$ /HTS-1 shifted toward high binding energy, suggesting that there was more electrons transfer from Ti to O by the introduction of  $\text{CuCl}_2$  species. The Gaussian values used in the curve resolution of the Ti 2p<sub>3/2</sub> peaks show that the one at lower binding energy (ca. 458.5 eV) was assigned to the octahedrally coordinated  $\text{Ti}^{4+}$  sites, and the other one at higher binding energy (ca. 460.0 eV) was attributable to  $\text{Ti}^{4+}$  in the tetrahedral coordination [44]. The relative area ratio of the peak at 460.0 eV assigned to tetrahedral Ti–O<sub>4</sub> species, however, decreased with the loading of  $\text{CuCl}_2$  species, resulting from  $\text{CuCl}_2$ -modified HTS-1 combined with the surface  $\text{CuCl}_2$  species [5,45]. In the Cu 2p XPS spectra (Fig. 4C), a lower peak intensity of the Cu 2p is observed for 10 wt%  $\text{CuCl}_2$ /HTS-1 in comparison with  $\text{CuCl}_2$ /P25 with the same load of  $\text{CuCl}_2$ , which implies that most of the  $\text{CuCl}_2$  species anchored onto the inner surface of HTS-1. Meanwhile, the Cu element is of  $\text{Cu}^{2+}$  in  $\text{CuCl}_2$ /HTS-1 according to the Cu 2p<sub>1/2</sub> and Cu 2p<sub>3/2</sub> peaks at 934.8 eV and 955.1 eV [46] respectively, whereas the weak signal of  $\text{Cu}^+$  in  $\text{CuCl}_2$

for  $\text{CuCl}_2$ /P25 was also observed with the binding energies at 932.4 and 952.2 eV (This might be due to the surface  $\text{Cu}^{2+}$  reduction in the high-vacuum environment ( $10^{-10}$ – $10^{-9}$  Torr) during the XPS measurement [47,48]). Similarly, Fig. 4D shows the XPS spectra of the Cl 2p band for the  $\text{CuCl}_2$ -modified HTS-1 and P25 samples, and the peak intensity at 199.2 eV suggests that 10 wt%  $\text{CuCl}_2$ /HTS-1 has the lower chlorine content on the surface of HTS-1. Thus, filling  $\text{CuCl}_2$  species into nano-cavity of HTS-1 zeolite with Cu–O–Ti–O<sub>3</sub> bridges has dramatically altered the optical property of the samples. EPR is a sensitive technology for the determination of  $\text{CuCl}_2$  coordination. Compared with EPR spectrum of pure  $\text{CuCl}_2$  [49], the gap between  $g_{\parallel}$  and  $g_{\perp}$  values has widened for the  $\text{CuCl}_2$ /HTS-1 sample (Fig. S2). Meanwhile, obvious splitting structure was also observed, which indicated that  $\text{CuCl}_2$  could interact with HTS-1 support via occupying the vacancies of the HTS-1 surface by forming a stable Cu–O–Cl surface species [50]. On the basis of the solubility test, it can be deduced that isolated  $\text{Cu}^{2+}$  species are insoluble copper speciation that resulted from the interaction between  $\text{CuCl}_2$  and support. In addition, an asymmetry can still be found in the spectrum of  $\text{CuCl}_2$ /HTS-1 sample, suggesting that two different  $\text{Cu}^{2+}$  species are coexisted in the catalyst: isolated  $\text{Cu}^{2+}$  species and associated  $\text{Cu}^{2+}$  cluster. In order to further support the interaction between  $\text{CuCl}_2$  and support, a TPR measurement of a  $\text{CuCl}_2$ /HTS-1 sample was performed. TPR results (Fig. S3) show that the reduction of  $\text{Cu}^{2+}$  to  $\text{Cu}^+$  occurs at lower temperature (about  $360^\circ\text{C}$ ) for the HTS-supported catalyst prepared from  $\text{CuCl}_2$ , whereas the reduction of  $\text{Cu}^{2+}$  to  $\text{Cu}^+$  appears at temperatures higher than  $500^\circ\text{C}$  [51]. The position of the peak is similar to those observed in the reduction of  $\text{Al}_2\text{O}_3$ -,  $\text{SiO}_2$ -supported  $\text{CuCl}_2$  with the strong interaction [51].

The optical properties of the as-prepared samples were probed by UV-Vis diffuse reflectance. As shown in Fig. 5A, the silicate-1 zeolite

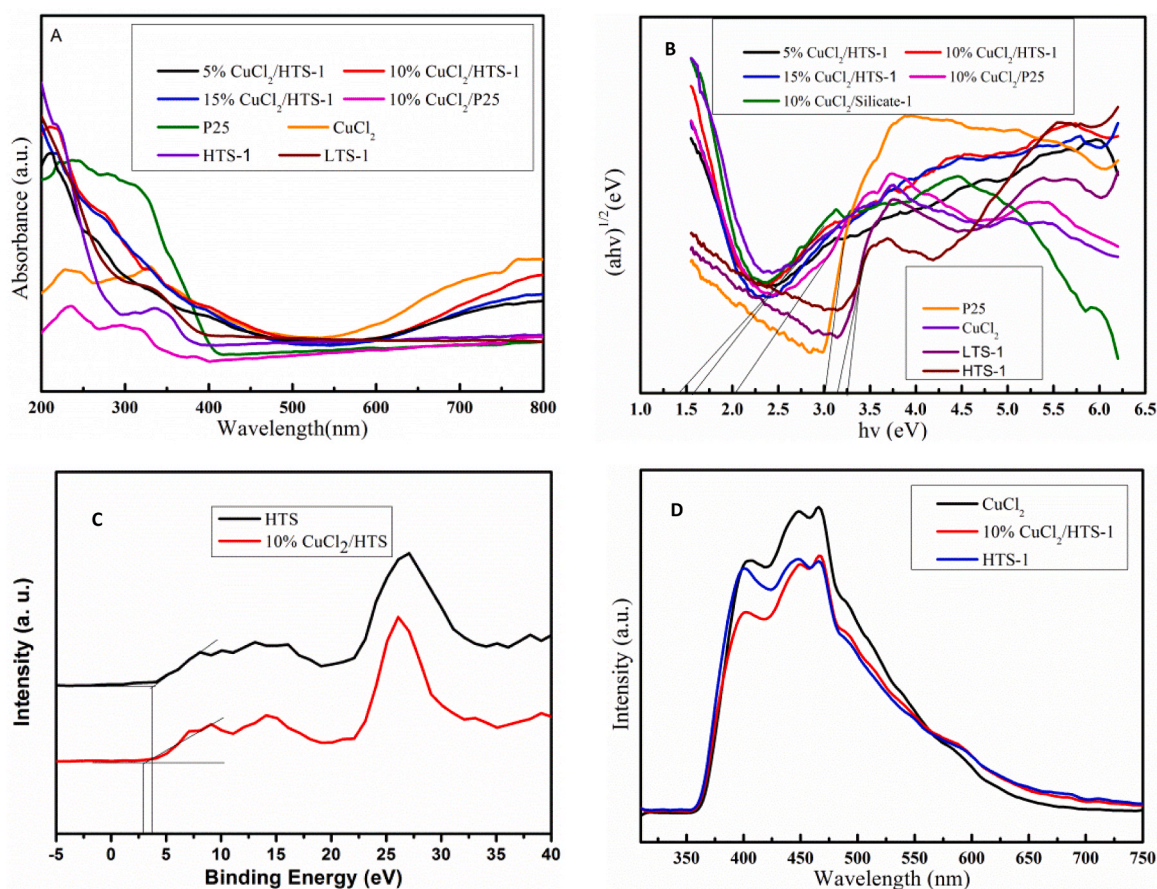


Fig. 5. UV-vis spectra of samples (A), tauc plots of samples for indirect band gap (B), valence band of HTS-1 and 10 wt%  $\text{CuCl}_2$ /HTS-1 samples (C), and photoluminescence spectra with the excitation wavelength of 290 nm (D).

without titanium species shows virtually no absorbance (Fig. S4), but the pristine HTS-1 zeolite exhibits two absorptions in the wavelength range of 200–380 nm. The 220 nm absorption arises from the charge transfer from  $O^{2-}$  to tetrahedral  $Ti^{4+}$  in the zeolite framework, and the ca. 300 nm absorption is attributable to extraframework Ti species in the HTS-1 [41,52]. The corresponding values of energy edge are 3.32 and 3.15 eV, which were exhibited only in the UV region. In comparison with those of the bulk  $TiO_2$  (P25, 3.03 eV), such a shift to the shorter wavelength in the absorption band for extraframework Ti species can be attributed to the size quantization effect of  $TiO_2$  nanoparticles, which is agreed well with XRD and Raman results [53]. After HTS-1 is doped with  $CuCl_2$  species, the absorption edges of  $CuCl_2$ /HTS-1 samples shift significantly to longer wavelengths as compared to HTS-1, clearly revealing that the absorption edges of  $CuCl_2$ /HTS-1 photocatalysts shift to the lower energy region. Meanwhile, a new visible absorption band appears at 600–800 nm for  $CuCl_2$ /HTS-1 samples, which is related to d-d electron transition of  $Cu^{2+}$  in  $CuCl_2$ . According to the “ $(ah\nu)^{1/2}$  versus photon energy” plots (Fig. 5B), the bandgap of HTS-1 and 10 wt%  $CuCl_2$ /HTS-1 is 3.15 eV and 1.69 eV, respectively, indicating that the latter is more capable of driving photocatalytic interaction under visible-light irradiation. Based on the VB XPS (Fig. 5C), the VBs for HTS-1 and 10 wt%  $CuCl_2$ /HTS-1 are revealed to be 3.66 and 2.74 eV, and the CBs for HTS-1 and 10 wt%  $CuCl_2$ /HTS-1 are calculated to be 0.51 eV and 1.05 eV, respectively. To further analyze the separation efficiency of photogenerated charge carriers in the photocatalyst, as-prepared HTS-1 zeolites were measured by room temperature photoluminescence (PL). As exhibited in Fig. 5D, three distinct emission peaks at 403, 452 and 467 nm are related to the emission of band gap transitions of HTS-1. Meanwhile, the  $CuCl_2$  also exhibit three strong emission peaks at 404, 449 and 465 nm, which might be attributed to the intrinsic luminescence properties of  $CuCl_2$ . In contrast, an obviously low PL intensity of  $CuCl_2$ -modified HTS-1 zeolites implies in presence of the interfacial transfer of photogenerated electrons from  $CuCl_2$  to HTS-1 zeolites, with retarding the charge recombination process. It's also worth noting that 10 wt%  $CuCl_2$ /HTS-1 is the lowest in PL intensity among the catalysts, indicating the highest ability in preventing the recombination of charge carriers. In addition, photoelectrochemical measurements were conducted to further confirm the separation efficiency of charge carriers (Fig. 6). The transient photocurrent responses of the samples reveal that  $CuCl_2$ /HTS-1 shows current intensity higher than pristine  $CuCl_2$  and HTS-1. The photocurrent enhancement of the  $CuCl_2$ /HTS-1 photocatalyst indicated the higher separation efficiency of the photoinduced electron-hole pairs and lower recombination rate, which resulted from the interaction of  $CuCl_2$  and HTS-1.

### 3.2. DFT calculations

To realize more clearly the electron and hole states of  $CuCl_2$ -

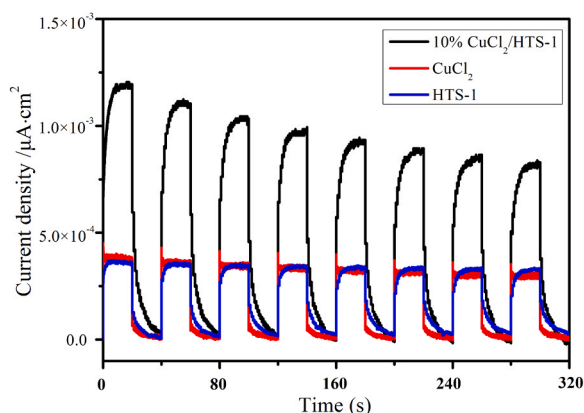


Fig. 6. Photocurrent response of HTS-1,  $CuCl_2$  and 10%  $CuCl_2$ /HTS-1 samples.

modified HTS-1 zeolites for the photocatalytic activation of aliphatic C–H bonds with complete selectivity of ketone and alcohol, three  $CuCl_2$ -modified HTS-1 models have been developed from the experimental results (Fig. 7): isolated  $CuCl_2$  on Ti sites (I), isolated  $CuCl_2$  on Si sites (II) and dimeric  $CuCl_2$  on Ti sites (III). Upon optimization, pure HTS-1 catalysts feature a tetrahedral environment about Ti sites with a Ti–O bond length of 1.803–1.859 Å, which are in agreement with the value of 1.793 Å reported from vacuo X-ray spectroscopies studies on TS-1 zeolites [54]. For the tetrahedral Ti sites by the introduction of  $CuCl_2$  (I and III), the Ti–O bond lengths of framework Ti sites change, indicating that relaxation around the tetrahedral Ti sites primarily occurs in the Si–O–Ti–O–Si chain. Particularly, one of the Ti–O bond lengths changes by 0.07 Å for the I, consistent with a more flexible structure. Notably, the distance of the corresponding O–Cu bond in the I is also shorter than those in the II and III, which suggests that the interaction of the isolated  $CuCl_2$  with the Ti sites is stronger. Therefore, the doping of isolated  $CuCl_2$  into tetrahedral Ti sites is predicted to be favorable. One reason could be that the isolated  $CuCl_2$ , which extra d electrons of  $Cu^{2+}$  would join in the hybridization and fill in the anti-bonding orbitals of Cu–O bonds in Si–O–Ti–O–Si chain, leads to the electron transfer from it to the O atom nearby. This result is also confirmed by the atomic Mulliken population analysis that the population of Cu atom on the I model is 0.453 e, and the populations are 0.365 e (II), 0.393 e (III) and 0.342 e ( $CuCl_2$ , Fig. S5). Comparing with the PDOS structure of the atom in the II and III models and pure  $CuCl_2$  (Fig. S6), the I introduced one strong hybridization peak between the Cl 2p, Ti 3d, O 2p and Cu 3d orbitals.

Furthermore, the excess electron and hole states by probing the highest occupied molecular orbital (HOMO) and the lowest unoccupied molecular orbital (LUMO) of the photocatalysts are investigated by our models, respectively (Fig. 8 and Fig. S5). In the HTS-1 models, the LUMO can be correlated with the tetrahedral  $Ti^{4+}$   $dz^2$  state. On the other hand, the HOMO predicted for the HTS-1 is comprised of the O (2p) orbitals of the silanol groups (Fig. 8). In contrast, the LUMOs associated with these isolated  $CuCl_2$ -modified HTS-1 structures are quite different in nature, which are delocalized over the  $CuCl_2$  moiety with the interaction of a Cu-based d orbital with the Cu–Cl antibonding orbital. Differently, the tetrahedral Ti–O groups in the I appears to make a contribution to the LUMO, and the state at the bottom of the conduction band is an unoccupied localized  $Ti^{4+}$  ( $d_{xy}$ ) with O 2p orbital. Meanwhile, the hybridization state of  $Cu^{2+}$  3d, Cl<sup>−</sup> 2p,  $O^{2-}$  2p and  $Ti^{4+}$  3d are predominant components of HOMO, which indicates that an excess electron is delocalized along the Cu–O bonds within the Cl–Cu–O–Ti–O chain in the I model. These results suggest that the introduction of isolated  $CuCl_2$  on Ti sites leads to a favorable electron trap on the Cu sites while the interactions of Ti with Cu site creates a good hole trap on the Ti sites (because introduction of Cu into adjacent Si sites is predicted to be unfavorable). Thus, a high degree of charge separation and a low rate of electron-hole pair recombination are formed on the low-doped  $CuCl_2$  samples, leading to an increase in photocatalytic activity. For the III, both LUMO and HOMO are composed mainly of a Cu 3d orbital and a  $\pi^*$  orbital of Cu–Cl group. However, the tetrahedral Ti sites in this structure appear to make no contribution to the LUMO. Therefore, the neighboring hole traps will readily quench the electron traps for the adjacent  $Cu^{2+}$  ( $d_{x^2-y^2}$ ) sites, resulting in a decrease in photocatalytic activity. This prediction is consistent with our preliminary experimental findings showing that the TOF values for the cyclohexane oxidation decreases almost linearly with increasing  $CuCl_2$  loading.

### 3.3. Photocatalytic performance

The photocatalytic performance of as-prepared  $CuCl_2$ /HTS-1 in  $CH_3CN$  was carried out on cyclohexane bearing unactivated  $sp^3$  C–H bonds as a representative alkane substrate under visible light irradiation (Table 1). Blank tests show that, no reaction product was detected under dark conditions or in the absence of photocatalysts (entries 1 and 12),

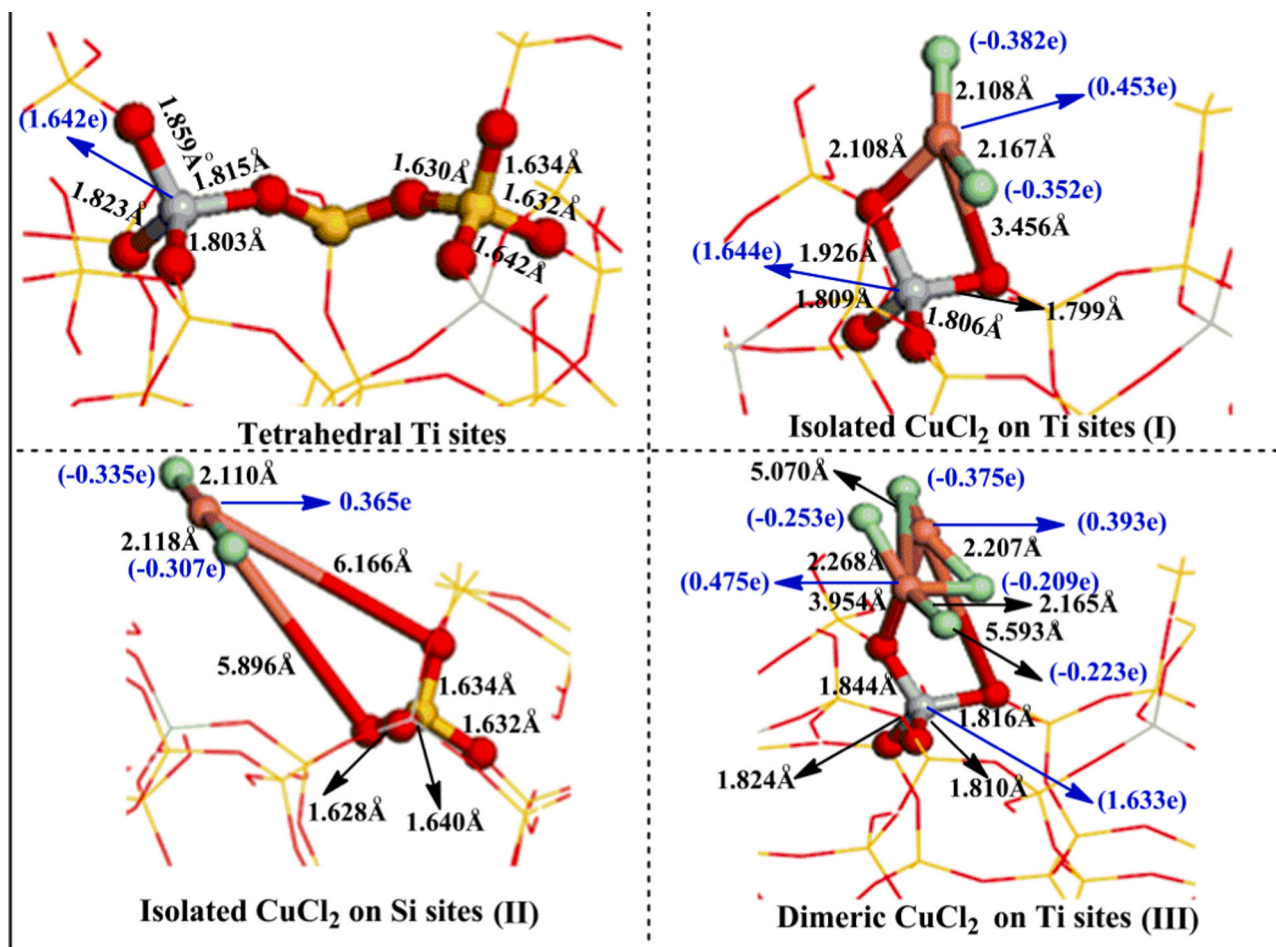


Fig. 7. Electronic structure of optimized models for Ti sites: isolated  $\text{CuCl}_2$  on Ti sites (I), isolated  $\text{CuCl}_2$  on Si sites (II) and dimeric  $\text{CuCl}_2$  on Ti sites (III).

confirming that both the light irradiation and photocatalyst were indispensable for selective transformation of cyclohexane. As it is seen, only 0.4% cyclohexane conversion is obtained in presence of pure HTS-1 zeolite (entry 2), however, the oxidation products are cyclohexanone and cyclohexanol as the sole products (cyclohexanone/cyclohexanol molar ratio = 2.3) under such conditions. Compared with the bulk  $\text{TiO}_2$ , no total oxidation products ( $\text{CO}_2$  and  $\text{H}_2\text{O}$ ) confirm the high catalytic selectivity of the isolated Ti species loaded in silica structure. To improve the photocatalytic activity of HTS-1 zeolite, we screened HTS-1 zeolite loaded with the different metal chlorides for the photo-oxidation of cyclohexane in the same condition (entries 5–11), in which some metal chlorides in presence of concentrated HCl show the photocatalytic activity in oxidation of cyclohexane reported in previous papers. Among these photocatalysts,  $\text{CuCl}_2$ -modified HTS-1 exhibited the remarkably high visible-light photocatalytic activity and about 23.5% of cyclohexane conversion with a complete KA-oil selectivity (100%, cyclohexanone/cyclohexanol molar ratio = 1.3) after 4 h (entry 4). To compare the oxidation activity of these catalysts with that of the non-supported metal chlorides, we tested  $\text{CuCl}_2$  as homogeneous catalysts in this reaction (entry 3). Obviously, low photocatalytic activity with the amount of chlorocyclohexane was obtained under similar conditions, which indicates that there exists a synergistic effect between  $\text{CuCl}_2$  and HTS-1 zeolite, which is beneficial to the oxidation of cyclohexane and the formation of KA-oil. Meanwhile, it is noted that the formation of the spin delocalized hybridization state of  $\text{Cu}^{2+}$  3d,  $\text{Cl}^-$  2p,  $\text{O}^{2-}$  2p and  $\text{Ti}^{4+}$  3d positioned within the VB by theoretical calculations (Fig. 8), as compared with the localized  $\text{O}^{2-}$  2p state at the bottom of the VB for HTS-1, should facilitate the charge separation of photogenerated carriers. Therefore, we tested the activity of a sample of mechanically

mixed  $\text{CuCl}_2$  and HTS-1 zeolite (10 wt% of  $\text{CuCl}_2$ ), and the cyclohexane conversion is only one-half of that of 10 wt%  $\text{CuCl}_2$  (entry 13), with producing a quantity of chlorocyclohexane by-products. These results further confirm that the self-formed unique structure with a favourable electronic influence (as demonstrated by XPS, Raman and UV-Vis) is essential for the high activity and selectivity.

With respect to the influence of the spatial distributions Ti sites on catalytic performance,  $\text{CuCl}_2$ -modified pure hollow silicate-1 and HTS-1 with low Ti content samples were investigated as the possible references. As shown in Table 2, it was found that the photocatalytic activities of both catalysts were lower than that of high Ti content sample (entries 1 and 2). Notably, bulk  $\text{TiO}_2$  (P25) supported  $\text{CuCl}_2$  species has also much lower activities, especially overoxidized product ( $\text{CO}_2$ ) was detected (entry 4). Thus, these findings imply that the combination of suitable Ti atom distribution and high surface density endows hollow-structure silicate with dramatically improved catalytic performance. Meanwhile, the high catalytic activity than solid-structured  $\text{CuCl}_2$ /TS-1 observed for the hollow-structured  $\text{CuCl}_2$ /HTS-1 is attributed to promote diffusion of hydrocarbon molecules and light absorption (entry 3). To elucidate whether the dispersion degree of the  $\text{CuCl}_2$  species is also a key factor in determining the photocatalytic activity, the turnover frequency values (TOF, cyclohexane conversion per Cu sites in the catalyst) are calculated, as shown in Table 2 (entries 5–7). The TOF values and ketone/alcohol molar ratio decreases almost linearly with increasing loading, indicating that  $\text{CuCl}_2$  catalyzes photocatalytic cycles more efficiently on lower-nuclearity sites. Additional investigations show that the  $\text{CuBr}_2$  or  $\text{CuI}$ -modified HTS-1 without Cl fail to improve the reaction, giving 0.2% of cyclohexane conversion under the equivalent irradiation. Furthermore, adding 0.1 mL of concentrated HCl as Cl sources to the reaction

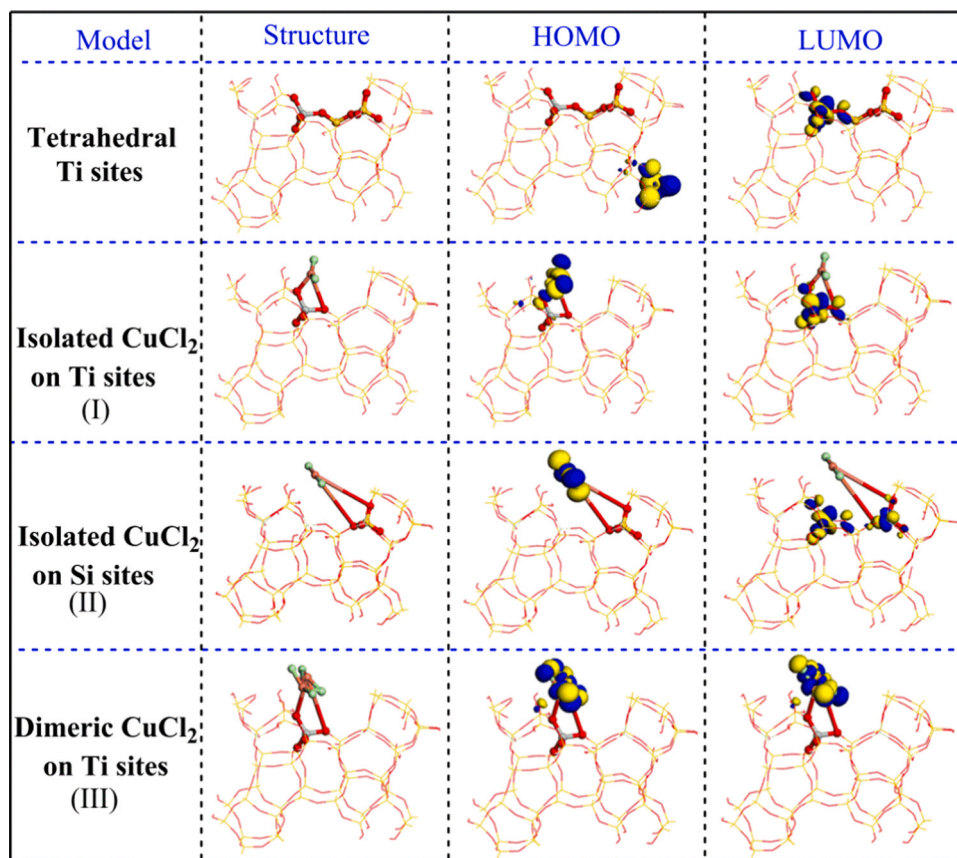
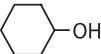
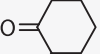


Fig. 8. HOMO and LUMO of Ti sites: isolated  $\text{CuCl}_2$  on Ti sites (I), isolated  $\text{CuCl}_2$  on Si sites (II) and Dimeric  $\text{CuCl}_2$  on Ti sites (III).

Table 1

The effect of catalytic oxidation of cyclohexane with different catalysts<sup>a</sup>.

Entry	Catalyst	Conv. (%)	Selectivity (%)	Ketone/alcohol molar ratio		TOF ( $\text{h}^{-1}$ )
			<div>   </div>			
1	Without	0	–	–	–	–
2	HTS-1	0.4	30.0	70.0	2.3	–
3	$\text{CuCl}_2$	10.1	40.1	52.7	1.3	5.1
4	10% $\text{CuCl}_2$ /HTS-1	23.5	43.5	56.5	1.3	12.0
5	10% $\text{SnCl}_2$ /HTS-1	2.0	54.7	45.3	0.8	1.4
6	10% $\text{NiCl}_2$ /HTS-1	2.1	44.0	56.0	1.3	1.5
7	10% $\text{FeCl}_3$ /HTS-1	1.6	42.7	56.4	1.3	0.8
8	10% $\text{CeCl}_3$ /HTS-1	1.8	41.9	58.1	1.4	2.0
9	10% $\text{AlCl}_3$ /HTS-1	0.6	37.6	62.4	1.7	0.2
10	10% $\text{MgCl}_2$ /HTS-1	0.4	32.0	68.0	2.1	0.1
11	10% $\text{CrCl}_3$ /HTS-1	0.2	34.0	66.0	1.9	0.1
12 <sup>b</sup>	10% $\text{CuCl}_2$ /HTS-1	0	–	–	–	–
13 <sup>c</sup>	10% $\text{CuCl}_2$ -HTS-1	11.4	35.6	50.4	1.7	3.9

<sup>a</sup> Reaction conditions: 0.5 g cyclohexane, 0.05 g catalyst, 12 mL acetonitrile,  $T = 40^\circ\text{C}$ ;  $t = 4$  h, 1.0 MPa  $\text{O}_2$


<sup>b</sup> Without light irradiation

<sup>c</sup> A sample of mechanically mixed  $\text{CuCl}_2$  and HTS-1 zeolite (10 wt% of  $\text{CuCl}_2$ )

system did not significantly promote this photocatalytic reaction (entry 10), with giving a quantity of chlorocyclohexane by-products. These data suggest that the Cl in  $\text{CuCl}_2$  is necessary and enough to efficiently enhance catalytic activity. In order to understand the product distribution in photooxidation of cyclohexane, we studied the effect of the

reaction parameters. (1) A larger amount of photocatalysts tended to inhibit the photo-oxidation reaction. Possibly the absorption of light is screened by excess  $\text{CuCl}_2$ /HTS-1 particles that masks part of the photosensitive surface, thereby preventing photoactivation (Table S2). (2) Under  $\text{N}_2$  atmosphere, there is no detection of KA-oil products,

**Table 2**The effect of catalytic oxidation of cyclohexane with different carrier.<sup>a</sup>

Entry	Catalyst	Conv. (%)	Selectivity (%)		Ketone/alcohol molar ratio	TOF (h <sup>-1</sup> )
						
1	10% CuCl <sub>2</sub> /LTS-1	17.7	39.7	60.3	1.5	9.1
2	10% CuCl <sub>2</sub> /Silicate-1	7.3	45.2	54.8	1.2	3.7
3	10% CuCl <sub>2</sub> /TS-1	13.6	29.3	70.6	2.4	6.9
4	10% CuCl <sub>2</sub> /P25	12.2	35.2	60.8	1.6	6.2
5	5% CuCl <sub>2</sub> /HTS-1	14.3	40.5	59.5	1.5	14.6
6	15% CuCl <sub>2</sub> /HTS-1	18.0	52.3	47.7	1.3	6.1
7	20% CuCl <sub>2</sub> /HTS-1	9.9	52.9	47.3	0.9	2.5
8	10% CuBr <sub>2</sub> /HTS-1	0.2	16.7	83.3	0.9	0.1
9	10% CuI/HTS-1	0.2	100	–	–	0.1
10 <sup>b</sup>	10% CuCl <sub>2</sub> /HTS-1	19.6	43.4	51.5	1.2	10.0
11 <sup>c</sup>	10% CuCl <sub>2</sub> /HTS-1	–	–	–	–	–
12 <sup>d</sup>	10% CuCl <sub>2</sub> /HTS-1	15.5	–	100	–	7.9

<sup>a</sup> Reaction conditions: 0.5 g cyclohexane, 0.05 g catalyst, 12 mL acetonitrile, T = 40 °C, t = 4 h, 1.0 MPa O<sub>2</sub><sup>b</sup> Adding 0.1 mL of concentrated HCl<sup>c</sup> Under N<sub>2</sub> atmosphere<sup>d</sup> Using cyclohexanol as the reactant.

indicating O<sub>2</sub> is indispensable (Table 2, entry 11). A promotion effect of increasing O<sub>2</sub> pressure on conversion and cyclohexanone selectivity was observed (Table S3), with preventing the formation of chlorocyclohexane by-products. Owing to the presence of an ample O<sub>2</sub> supply, the possibility of the reaction by chlorine radicals and alkyl radicals to form alkyl halides products is suppressed. (3) The low conversion of cyclohexane at first indicates a short induction period, which most likely relates to initiation of the radical reaction. Longer reaction time led to a higher conversion of cyclohexane (Table S4). No hydroperoxide intermediates was detected by iodometric titration, which indicates that these possible intermediates are quickly transformed into more stable cyclohexanone or cyclohexanol. (4) To study the catalytic stability, we separated the solid catalysts (10 wt% CuCl<sub>2</sub>/HTS-1) from the reaction mixtures after a reaction time of 4 h, and the reused catalyst (six times) exhibited the activity similar to 10 wt% CuCl<sub>2</sub>/HTS-1 (Fig. S7).



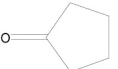
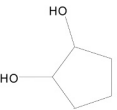

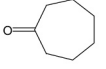
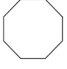
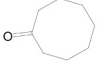
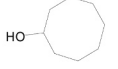

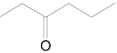
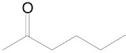
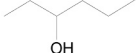
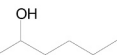

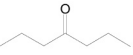
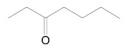
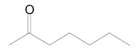
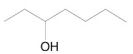
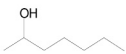
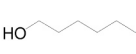
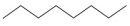
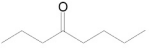
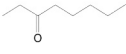
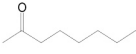
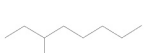

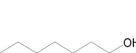
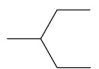
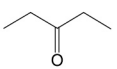
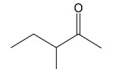
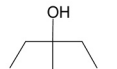
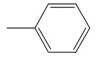
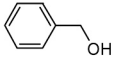
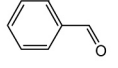
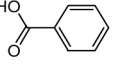
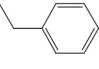
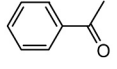
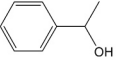
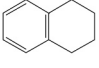
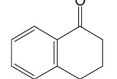
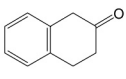
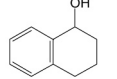
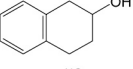
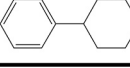
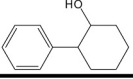
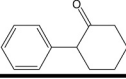
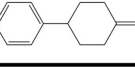
Encouraged by the excellent photo-catalytic performance of CuCl<sub>2</sub>/HTS-1 in the photo-oxidation of cyclohexane to KA-oil, we proceeded to investigate the scope of this reaction (Table 3). Firstly, we test cycloalkanes to the corresponding ketones and alcohols. Smaller sized cycloalkanes such as cyclopentane could be oxidized in low conversion (6.2%) with 67.7% selectivity of ketone and alcohol, along with o-diol (28.0%) occurs. Similar to cyclohexane, larger ones (cycloheptane and cyclooctane) were efficiently converted into their corresponding products in excellent conversion (19.5% and 18.8%). Meanwhile, a higher chemoselectivity of ketone and alcohol than cyclohexane is observed, particularly with the cycloheptanone being formed in 91.9% chemoselectivity from cycloheptane. Next, several linear alkanes were subjected to the photo-oxidation under these reaction conditions. Photo-oxidation of n-hexane with 10% CuCl<sub>2</sub>/HTS-1 gave an approximate 1:1 regioisomeric mixture of 2-ketone (alcohol) and 3-ketone (alcohol) at 13.0% conversion. Under visible-light irradiation, 9.2% n-heptane and 15.9% n-octane can also be transformed into the corresponding oxidized products, respectively. Interesting, the more unactivated primary than secondary C–H bonds in longer carbon chain alkanes also react to give the corresponding 1-alcohol chemoselectivity (about 10%). The branched alkane such as 3-methyl pentane give 8.8% conversion, a β-scission of a 3-methyl-3-oxypentan radical to pentan-3-one as a major product (56.5%) along with 3-methylpentan-3-ol (16.7%) occurs, which is due to the fact that the β-scission of the tertiary-carbon oxy-radical

occurs easily [55]. Finally, the protocol was extended for the photo-oxidation of various alkylbenzenes. It was found that the 10% CuCl<sub>2</sub>/HTS-1 exhibits high efficiency for 1 position oxidation of tetrahydronaphthalene with 87.6% selectivity to the corresponding products at 26.0% conversion. Interesting, oxygenation at the secondary C–H bond of cyclohexylbenzene was favored, ortho and para products (ortho/para molar ratio = 7.6) were formed in 100% selectivity when the more activated tertiary C–H bond at benzylic position with steric hindrance is unavailable. Notably, under identical conditions, 10% CuCl<sub>2</sub>/HTS-1 does not present high photocatalytic activity in the oxidation of toluene and ethylbenzene, which is surprising in view of the fact that toluene hydrocarbons with weaker C–H bonds (85 kcal mol<sup>-1</sup> versus 94 kcal mol<sup>-1</sup> [56] and lower ionization potentials (8.8 eV versus 9.8 eV [57]) than cyclohexane. A plausible explanation would be the fact that these toluene hydrocarbons reside preferentially at Ti or Cu cation sites in the hollow HTS-1 zeolite cage [4,58] restrictions to hopping among cations may prevent occupation and turnover of unsaturated hydrocarbons at radical defect sites, while alkanes show no preference for trajectories along cation sites of HTS-1 zeolite. Furthermore, when applied to the oxygen functionalization of 2-hexanone and n-hexanenitrile, CuCl<sub>2</sub>/HTS-1 only provided trace amounts of the oxidized product, indicating that the C–H bond adjacent to electron withdrawing groups were not amenable to this protocol.

#### 3.4. Active sites related to the reaction mechanism

The excellent photocatalytic activity of CuCl<sub>2</sub>/HTS-1 for selective oxygenation of alkanes to ketone/alcohol can be explained by the combination of heterojunction interface and hollow sphere-like structure. The hollow structure for HTS-1 is formed after sulfuric acid treatment of traditional solid TS-1 via a dissolution-recrystallization process (Scheme 1). Firstly, the Si–O–Si and Si–O–Ti bridging bonds inside of the TS-1 crystals gradually dissolves in the presence of OH<sup>-</sup> from TPAOH. On the other hand, the nucleation of silica dissolved from the inside of the crystals occurs with the increase of Si content. However, a lower concentration of OH<sup>-</sup> from firstly treatment by sulfuric acid leads to a slower rate of nucleation, thus a large intraparticle voids inside zeolite is created by the recrystallization process. It is probably due to its intra-particle voids of HTS-1, which can enhance the accessibility

**Table 3**  
Catalytic oxidation of different alkanes and alkylarenes.<sup>a</sup>

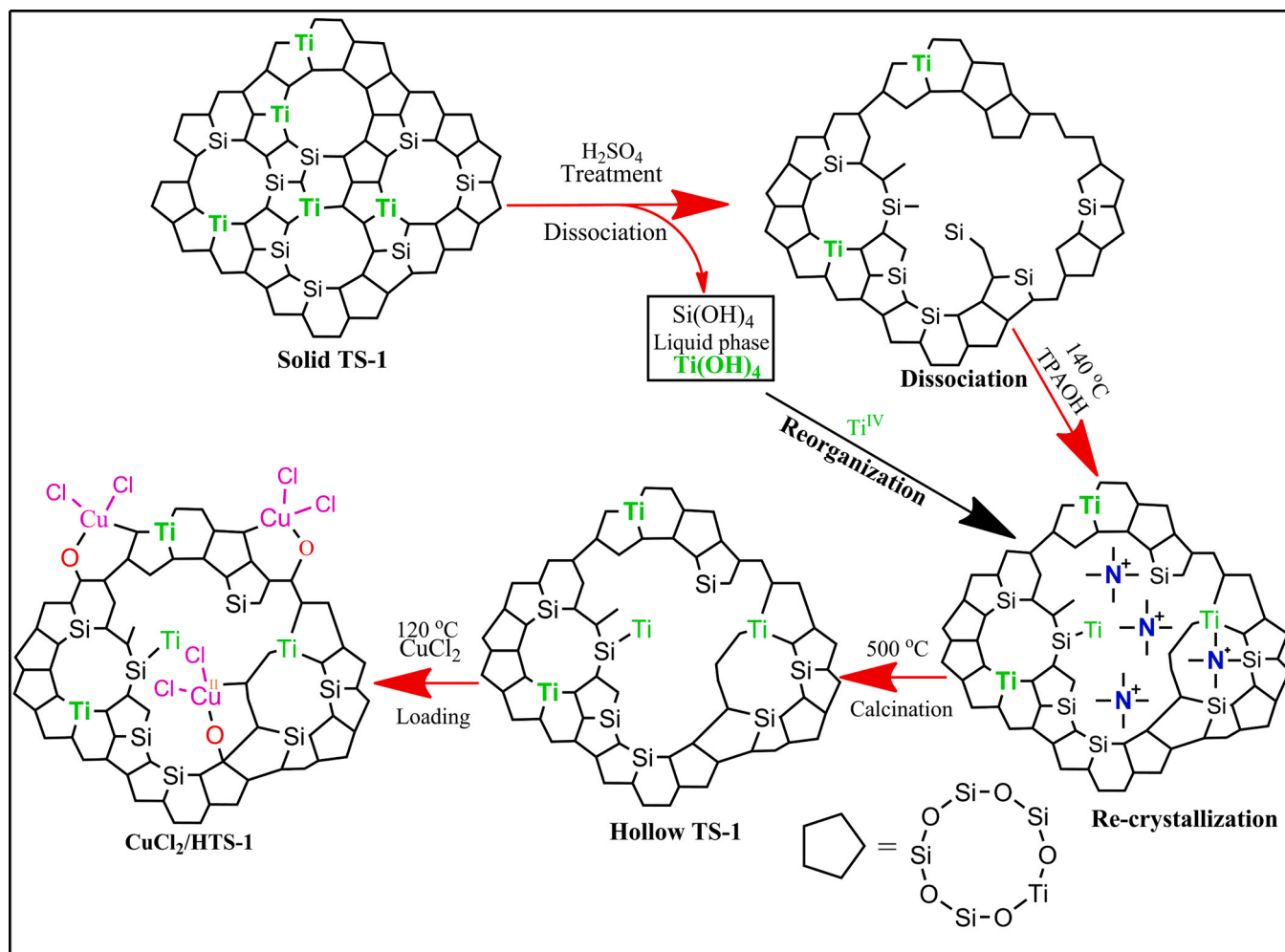
Substrate	Conv. (%)	Sele. (%)			
	6.2	 19.3	 48.4	 28.0	
	19.5	 91.9			
	18.8	 59.2	 22.1		
	13.0	 24.8	 18.8	 11.1	
		 29.0			
	9.2	 10.6	 19.0	 19.9	
		 8.3	 9.9	 15.5	
	15.9	 14.2	 18.9	 16.2	
		 8.3	 8.8	 12.0	
	8.8	 56.5	 6.0	 16.7	
	3.1	 8.3	 86.4	 4.9	
	6.1	 65.4	 22.1		
	26.0	 70.6	 5.6	 17.0	
		 6.8			
	16.2	 8.7	 79.9	 11.7	

<sup>a</sup> Reaction conditions: 0.5 g substrate, 0.05 g catalyst, 12 mL acetonitrile, t = 4 h, T = 40 °C, 1.0 MPaO<sub>2</sub>.

of active centers and diffusion of product molecules throughout the shell of the catalysts. In addition, the dissolved Ti species can be regrown onto the surface of HTS-1 crystals and the Ti species on the surface are more accessible than those in the core of the solid-structured TS-1 crystals. Secondly, the loading of CuCl<sub>2</sub> species onto the surface of HTS-1 through Cu–O–Si interaction is essential for their initial and sustained high reactivity in photocatalysis, since the CuCl<sub>2</sub> species can adsorb visible-light and the formation of the heterojunction interface exposed at the crystalline surfaces. Thus, a built-in electric field formed in the hollow CuCl<sub>2</sub>/HTS-1 heterojunction made the electrons diffuse toward the Ti<sup>4+</sup> sites (inner shell) while the holes diffused toward the CuCl<sub>2</sub> (outer shell),

leading to directed charge separation and transport spatially. As a result, the advantages of hollow structures for charge separation and transport mainly include two aspects: 1) a thin shell of the hollow structure largely reduces the migration distance of photoexcited charge carriers; 2) the directed charge separation and transfer through the construction of hollow-structured heterojunctions on their inner and outer surfaces.

To explore the reaction mechanism, quenching experiments with the addition of scavengers were performed to understand the role of the main reactive species for selective photo-reaction of alkanes under aerobic condition. Herein, the scavengers such as triethanolamine (TEOA), AgNO<sub>3</sub>, benzoquinone (BQ), dimethylbutadiene (DMBD) and

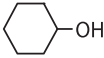
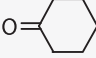


Scheme 1. Scheme of proposed structure (model) evolution.

isopropanol (IPA) are used to trap photogenerated positive holes ( $h^+$ ), photogenerated electrons ( $e^-$ ), superoxide anion radicals ( $\bullet O_2^-$ ), halogen ( $Cl\bullet$ ) and hydroxyl radicals ( $\bullet OH$ ), respectively. As shown in Table 4, when TEOA and  $AgNO_3$  were added to capture  $h^+$  and  $e^-$ , respectively [14,59], the conversion of cyclohexane is almost completely quenched. In contrast, the addition of DMBD as radical captures for  $Cl\bullet$  decreases significantly the cyclohexane conversions (5.7%) [60]. Furthermore, the quenching experiment involving IPA and BQ scavengers for  $\bullet OH$  and  $\bullet O_2^-$  shows that the cyclohexane conversion

only partly decreased compared to the other four scavengers. These results suggested that the  $h^+$ ,  $e^-$  and  $Cl\bullet$  are involved in the reaction, but  $h^+$  and  $e^-$  play an indispensable role in the first step of the cyclohexane partial oxidation. As a final piece of mechanistic insight, additional experiments were further carried out to probe the reaction mechanism. (1) Kinetic profiles showed that cyclohexane was quickly consumed after an induction period (Fig. S8, ca. 120 min), indicating that the radical-mediated mechanism may be prevailing. (2) Interference with a radical acceptor bis(pinacolato)diboron ( $B_2pin_2$ ) led to the lower

**Table 4**  
Reactive species trapping experiments of  $CuCl_2/HTS-1$  samples.<sup>a</sup>

Entry	Scavenger	Conv. (%)	Selectivity (%)	
				
1	TEOA	0.4	57.1	42.9
2	IPA	18.0	45.4	54.6
3	BQ	17.1	46.1	53.9
4	DMBD	5.7	38.8	61.2
5	$AgNO_3$	0.15	41.6	58.4

<sup>a</sup> Reaction conditions: 0.5 g cyclohexane, 0.05 g 10 wt%  $CuCl_2/TS-1$  catalyst, 12 mL acetonitrile, 1.0 MPa  $O_2$ ,  $T = 40\text{ }^\circ\text{C}$ ,  $t = 4\text{ h}$ , 10 mmol/L scavenger.

formation rate of KA-oils with 7.1% conversion, which are further strengthen the radical-mediated mechanism (Fig. S9). (3) Kinetic isotope effect (KIE) for the competitive oxidation of 1:1 cyclohexane/cyclohexane- $d_{10}$  from initial reaction rates was observed to be 2.1 (Fig. S9), suggesting that the C–H bond cleavage of cyclohexane to C-centered radical formation is high. (4) A cyclohexanol intermediate experiment show a 100% cyclohexanone selectivity with 15.5% conversion (Table 2), indicating that a consecutive reaction of formed cyclohexanol to cyclohexanone may occur simultaneously during the photocatalytic process. (5) KA-oil was obtained as the primary product, when the decomposition of cyclohexyl hydroperoxide intermediate on  $\text{CuCl}_2/\text{HTS-1}$  was tested under the same photoirradiation.

Combining all of the information presented herein [61], a possible photocatalytic mechanism is tentatively proposed, as shown in Fig. 9. For the  $\text{CuCl}_2/\text{HTS-1}$  photocatalyst, the bottom of the conduction band (CB) is contributed by the hybridization state of  $\text{Ti}^{4+}$  3d and  $\text{O}^{2-}$  2p orbitals, and the hybridization state of  $\text{Cu}^{2+}$  3d,  $\text{Cl}^-$  2p,  $\text{O}^{2-}$  2p and  $\text{Ti}^{4+}$  3d are predominant components of the top of the valence band (Fig. S6). These spin delocalized state contributes in reducing of recombination rates of excited charges with achieving the better separation of the photogenerated electron-hole pairs for the  $\text{CuCl}_2$  modified HTS-1, which is well consistent with its remarkably low PL intensity. The rich surface Ti sites— $\text{CuCl}_2$  species boundaries not only help to shorten the migration path, but also provide abundant  $[\text{Cu}^{2+}-\text{Cl}]$  units to directly capture the photogenerated holes for the formation of  $\text{Cl}\cdot$ . Meanwhile, the utilization efficiency of photogenerated holes is significantly elevated, which promotes photo-activation of the C–H bonds, endowing the  $\text{CuCl}_2/\text{HTS-1}$  with excellent photocatalytic performance in alkane oxidation. Under visible-light excitation, the electrons and holes are generated in the CB and VB of  $\text{CuCl}_2/\text{HTS-1}$  photocatalysts, respectively. The photogenerated holes oxidize the adsorbed alkane molecule in the zeolite surface to generate alkyl radical and  $\text{Cl}\cdot$ . The photoexcited electrons on the CB, which is more negative than the standard reduction potential of  $\text{E}(\text{H}_2\text{O}/\cdot\text{OH})$ , can be rapidly captured by  $\text{H}_2\text{O}$  to produce  $\cdot\text{OH}$  via electron transfer routes. Such these alkyl radical,  $\text{Cl}\cdot$  and  $\cdot\text{OH}$  radicals stabilized in the pores of HTS-1 zeolite are known to be able to abstract a hydrogen atom from saturated alkane to alkyl radical, benefiting the second step of photocatalytic alkane oxidation. Subsequently, the reaction of alkyl radicals with  $\text{O}_2$  results in the formation of alkylperoxyl radical, which can also abstract hydrogen atom from

another alkane molecule to form alkyl hydroperoxide and regenerate alkyl radical for the catalytic cycling pathway. Alkyl hydroperoxide decompose selectively in the presence of the framework Ti or Cu sites to cyclohexanone and cyclohexanol. In addition, another minor pathway via  $\cdot\text{OH}$  radicals coupling with alkyl radicals to product alcohols may also exist and the formed alcohols may be oxidized further to ketone by a consecutive reaction. Undoubtedly, in our work, maintaining the hollow zeolite cages as an example of photochemistry through the photocatalytic cycle might also be a key factor to obtain high activity and selectivity of ketone and alcohol [4,62]. The crucial function of the host (zeolite) in this case is motional constraints imposed on the proposed primary radical products ( $\text{Cl}\cdot$ ,  $\cdot\text{OH}$  and alkyl radical). This suppresses random radical coupling reactions or non-selective decomposition of alkyl hydroperoxide in liquid alkane autoxidation which otherwise would destroy product selectivity.

#### 4. Conclusion

In conclusion, we introduce the construction of hollowed zeolite (HTS-1)-based photocatalysts featuring isolated tetrahedral titanium sites that can efficiently interact with  $\text{CuCl}_2$  species. The data in Table S5 compare the results and other photocatalytic systems used for this reaction. The  $\text{CuCl}_2/\text{HTS-1}$  photocatalyst thus obtained show superior photocatalytic activities (24% conversion) for the selective C–H oxygenation of cyclohexane to KA-oil in complete selectivity (100%) using  $\text{O}_2$  under the irradiation of visible light. This heterogeneous photocatalyst system avoided the employment of any additional photosensitizer or cocatalyst, and the photocatalyst was found to be stable and recyclable for subsequent runs. The high performance of cyclohexane oxygenation of the photocatalyst can be attributed to the unique hollow structure of  $\text{CuCl}_2/\text{HTS-1}$  with the  $\text{Cu}-\text{O}-\text{Ti}-\text{O}_3$  heterojunctions, which improve its charge transfer and separation abilities for direct activation of the substrate and oxygen molecules. Moreover, the mild oxygenation reaction described here is exploited to be extended to a variety of alkylarene and alkane compounds possessing these inert C–H bonds for the synthesis of the corresponding alcohols and ketones.

#### CRediT authorship contribution statement

Hui Yin: Investigation, Methodology, Software, Validation, Writing

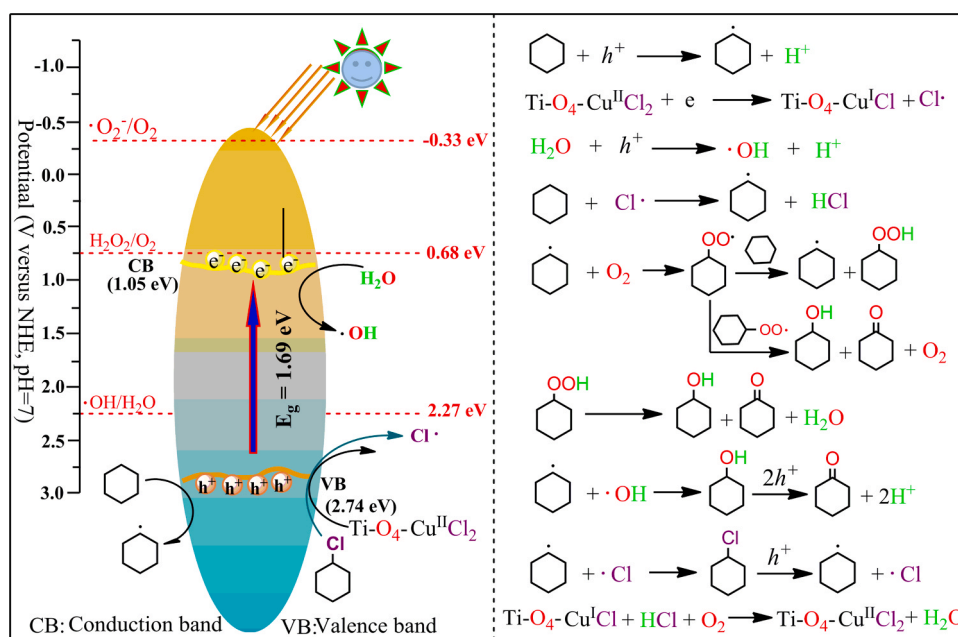


Fig. 9. Mechanism for the photooxidation of cyclohexane with  $\text{O}_2$  over the  $\text{CuCl}_2/\text{HTS-1}$  photocatalyst.

– original draft. **Feng Su**: Formal analysis, Investigation, Writing – review & editing. **Chao Luo**: Investigation, Resources, Writing – review & editing. **Lixia Zhu**: Formal analysis, Methodology, Visualization. **Wenzhou Zhong**: Conceptualization, Formal analysis, Funding acquisition, Project administration, Supervision, Software, Visualization, Writing – review & editing. **Liqiu Mao**: Data curation, Funding acquisition, Project administration, Supervision, Visualization, Writing – review & editing. **Kuiyi You**: Formal analysis, Software, Writing – review & editing. **Dulin Yin**: Data curation, Formal analysis, Writing – review & editing.

## Declaration of Competing Interest

The authors declare that they have no known competing financial interests or personal relationships that could have appeared to influence the work reported in this paper.

## Acknowledgements

This work was supported by the Natural Science Foundation of China (Grant No.21978078, 21878074 and 21576078) and Collaborative Innovation Center of New Chemical Technologies for Environmental Benignity and Efficient Resource Utilization.

## Appendix A. Supporting information

Supplementary data associated with this article can be found in the online version at [doi:10.1016/j.apcatb.2021.120851](https://doi.org/10.1016/j.apcatb.2021.120851).

## References

- [1] U. Schuchardt, D. Cardoso, R. Sercheli, R. Pereira, R. Cruz, M. Guerreiro, D. Mandelli, E. Spinacé, Cyclohexane oxidation continues to be a challenge, *Appl. Catal. A Gen.* 211 (2001) 1–17, [https://doi.org/10.1016/S0926-860X\(01\)00472-0](https://doi.org/10.1016/S0926-860X(01)00472-0).
- [2] F. Cavani, G. Centi, S. Perathoner, F. Trifiro, *Sustainable Industrial Processes*, Wiley-VCH, Weinheim, 2009, pp. 331–391.
- [3] W. Gu, M. Warrier, V. Ramamurthy, R.G. Weiss, Photo-Fries reactions of 1-naphthyl esters in cation-exchanged zeolite Y and polyethylene media, *J. Am. Chem. Soc.* 121 (1999) 9467–9468, <https://doi.org/10.1021/ja990818o>.
- [4] H. Sun, F. Blatter, H. Frei, Cyclohexanone from cyclohexane and O<sub>2</sub> in a zeolite under visible light with complete selectivity, *J. Am. Chem. Soc.* 118 (1996) 6873–6879, <https://doi.org/10.1021/ja953273g>.
- [5] W.Z. Zhong, T. Qiao, J. Dai, L.Q. Mao, Q. Xu, G.Q. Zou, X.X. Liu, D.L. Yin, F. P. Zhao, Visible-light-responsive sulfated vanadium-doped TS-1 with hollow structure: enhanced photocatalytic activity in selective oxidation of cyclohexane, *J. Catal.* 330 (2015) 208–221, <https://doi.org/10.1016/j.jcat.2015.06.013>.
- [6] A. Ebadi, N. Safari, M.H. Peyrovi, Aerobic oxidation of cyclohexane with  $\gamma$ -alumina supported metallophthalocyanines in the gas phase, *Appl. Catal. A Gen.* 321 (2007) 135–139, <https://doi.org/10.1016/j.apcata.2007.01.040>.
- [7] G.T. Zhang, C.L. Bian, A.W. Lei, Advances in visible light-mediated oxidative coupling reactions, *Chin. J. Catal.* 36 (2015) 1428–1439, [https://doi.org/10.1016/S1872-0667\(15\)60885-3](https://doi.org/10.1016/S1872-0667(15)60885-3).
- [8] C. Wang, Y.C. Hou, J.J. Cheng, M.J. Lin, X.C. Wang, Biomimetic donor-acceptor motifs in carbon nitrides: enhancing red-light photocatalytic selective oxidation by rational surface engineering, *Appl. Catal. B Environ.* 294 (2021) 120259–120267, <https://doi.org/10.1016/j.apcatb.2021.120259>.
- [9] P. Peng, L. Peng, G. Wang, F. Wang, Y. Luo, A. Lei, Visible light mediated aerobic radical C–H phosphorylation toward arylphosphonates, *Org. Chem. Front.* 3 (2016) 749–752, <https://doi.org/10.1039/c6qo00049e>.
- [10] J. He, L. Chen, D. Ding, Y.K. Yang, C.T. Au, S.F. Yin, Facile fabrication of novel Cd<sub>3</sub>(C<sub>3</sub>N<sub>3</sub>S<sub>3</sub>)<sub>2</sub>/CdS porous composites and their photocatalytic performance for toluene selective oxidation under visible light irradiation, *Appl. Catal. B Environ.* 233 (2018) 243–249, <https://doi.org/10.1016/j.apcatb.2018.04.008>.
- [11] F. Ding, P. Chen, F. Liu, L. Chen, J.K. Guo, S. Shen, Q. Zhang, L.H. Meng, C.T. Au, S. F. Yin, Bi<sub>2</sub>MoO<sub>6</sub>/g-C<sub>3</sub>N<sub>4</sub> of 0D/2D heterostructure as efficient photocatalyst for selective oxidation of aromatic alkanes, *Appl. Surf. Sci.* 490 (2019) 102–108, <https://doi.org/10.1016/j.apsusc.2019.06.057>.
- [12] D. Hu, V.V. Ordonsky, A.Y. Khodakov, Major routes in the photocatalytic methane conversion into chemicals and fuels under mild conditions, *Appl. Catal. B Environ.* 286 (2021) 119913–119931, <https://doi.org/10.1016/j.apcatb.2021.119913>.
- [13] L.-H. Wei, C.-D. Wu, Incorporation of Fe-phthalocyanines into a porous organic framework for highly efficient photocatalytic oxidation of arylalkanes, *Appl. Catal. B Environ.* 234 (2018) 290–295, <https://doi.org/10.1016/j.apcatb.2018.04.055>.
- [14] L.P. Xiang, J.J. Fan, W.Z. Zhong, L.Q. Mao, K.Y. You, D.L. Yin, Heteroatom-induced band-reconstruction of metal vanadates for photocatalytic cyclohexane oxidation towards KA-oil selectivity, *Appl. Catal. A Gen.* 575 (2019) 120–131, <https://doi.org/10.1016/j.apcata.2019.02.015>.
- [15] P. Wen, Y. Zhang, G. Xu, D. Ma, P. Qiu, X.X. Zhao, Ti<sup>3+</sup> self-doped TiO<sub>2</sub> as a photocatalyst for cyclohexane oxidation under visible light irradiation, *J. Mat.* 5 (2019) 696–701, <https://doi.org/10.1016/j.jmat.2019.04.009>.
- [16] Y. Shiraishi, S. Shiota, H. Hirakawa, S. Tanaka, S. Ichikawa, T. Hirai, Titanium dioxide/reduced graphene oxide hybrid photocatalysts for efficient and selective partial oxidation of cyclohexane, *ACS Catal.* 7 (2016) 293–300, <https://doi.org/10.1021/acscatal.6b02611>.
- [17] H. Li, T.X. Zhang, C. Pan, C.C. Pu, Y. Hu, X.Y. Hu, E.Z. Liu, J. Fan, Self-assembled Bi<sub>2</sub>MoO<sub>6</sub>/TiO<sub>2</sub> nanofiber heterojunction film with enhanced photocatalytic activities, *Appl. Surf. Sci.* 391 (2017) 303–310, <https://doi.org/10.1016/j.apsusc.2016.06.167>.
- [18] D.X. Yang, T.B. Wu, C.J. Chen, W.W. Guo, H.Z. Liu, B.X. Han, The highly selective aerobic oxidation of cyclohexane to cyclohexanone and cyclohexanol over V<sub>2</sub>O<sub>5</sub>@TiO<sub>2</sub> under simulated solar light irradiation, *Green Chem.* 19 (2017) 311–318, <https://doi.org/10.1039/c6gc02748b>.
- [19] W.J. Ren, Z.H. Ai, F.L. Jia, L.Z. Zhang, X.X. Fan, Z.G. Zou, Low temperature preparation and visible light photocatalytic activity of mesoporous carbon-doped crystalline TiO<sub>2</sub>, *Appl. Catal. B Environ.* 69 (2007) 138–144, <https://doi.org/10.1016/j.apcatb.2006.06.015>.
- [20] M.A. Nadeem, H. Idriss, Effect of temperature on the photoreactions of ethanol over Ag/TiO<sub>2</sub> in steady state catalytic conditions, *Appl. Catal. B Environ.* 284 (2021) 119736–119744, <https://doi.org/10.1016/j.apcatb.2020.119736>.
- [21] X. Bao, H. Li, Z. Wang, F. Tong, M. Liu, Z. Zheng, P. Wang, H. Cheng, Y. Liu, Y. Dai, Y. Fan, Z. Li, B. Huang, TiO<sub>2</sub>/Ti<sub>3</sub>C<sub>2</sub> as an efficient photocatalyst for selective oxidation of benzyl alcohol to benzaldehyde, *Appl. Catal. B Environ.* 286 (2021), 119885, <https://doi.org/10.1016/j.apcatb.2021.119885M>.
- [22] G.Q. Zou, W.Z. Zhong, L.Q. Mao, Q. Xu, J.F. Xiao, D.L. Yin, Z.S. Xiao, S.R. Kirk, T. Shu, A non-nitric acid method of adipic acid synthesis: organic solvent- and promoter-free oxidation of cyclohexanone with oxygen over hollow-structured Mn/TS-1 catalysts, *Green Chem.* 17 (2015) 1884–1892, <https://doi.org/10.1039/c4gc02333a>.
- [23] G. Ricchiardi, A. Damin, S. Bordiga, C. Lamberti, G. Spano, F. Rivetti, A. Zecchina, Vibrational structure of titanium silicate catalysts. A spectroscopic and theoretical study, *J. Am. Chem. Soc.* 123 (2001) 11409–11419, <https://doi.org/10.1021/ja010607v>.
- [24] G.H. Li, N.M. Dimitrijevic, L. Chen, J.M. Nichols, T. Rajh, K.A. Gray, The important role of tetrahedral Ti<sup>4+</sup> sites in the phase transformation and photocatalytic activity of TiO<sub>2</sub> nanocomposites, *J. Am. Chem. Soc.* 130 (2008) 5402–5403, <https://doi.org/10.1021/ja711118u>.
- [25] M. Anpo, J.M. Thomas, Single-site photocatalytic solids for the decomposition of undesirable molecules, *Chem. Commun.* 31 (2006) 3273–3278, <https://doi.org/10.1039/b606738g>.
- [26] T.R. Eaton, M.P. Campos, K.A. Gray, J.M. Notestein, Quantifying accessible sites and reactivity on titania-silica (photo)catalysts: Refining TOF calculations, *J. Catal.* 309 (2014) 156–165, <https://doi.org/10.1016/j.jcat.2013.09.015>.
- [27] X.B. Chen, S. Shen, L.J. Guo, S.S. Mao, Semiconductor-based photocatalytic hydrogen generation, *Chem. Rev.* 110 (2010) 6503–6570, <https://doi.org/10.1021/cr1001645>.
- [28] R.Y. Ma, W. Chen, L. Wang, X.F. Yi, Y. Xiao, X.H. Gao, J. Zhang, X.M. Tang, C. G. Yang, X.J. Meng, A.M. Zheng, F.S. Xiao, N-oxyl radicals trapped on zeolite surface accelerate photocatalysis, *ACS Catal.* 9 (2019) 10448–10453, <https://doi.org/10.1021/acscatal.9b03737>.
- [29] F. Blatter, H. Sun, S. Vasenkov, H. Frei, Photocatalyzed oxidation in zeolite cages, *Catal. Today* 41 (1998) 297–309, [https://doi.org/10.1016/S0920-5861\(98\)00021-2](https://doi.org/10.1016/S0920-5861(98)00021-2).
- [30] K. Takaki, J. Yamamoto, K. Komeyama, T. Kawabata, K. Takehira, Photocatalytic oxidation of alkanes with dioxygen by visible light and Copper(II) and Iron(III) chlorides: preference oxidation of alkanes over alcohols and ketones, *Bull. Chem. Soc. Jpn.* 77 (2004) 2251–2255, <https://doi.org/10.1246/bcsj.77.2251>.
- [31] W. Wu, X. He, Z. Fu, Y. Liu, Y. Wang, X. Gong, X. Deng, H. Wu, Y. Zou, N. Yu, D. Yin, Metal chlorides-catalyzed selective oxidation of cyclohexane by molecular oxygen under visible light irradiation, *J. Catal.* 286 (2012) 6–12, <https://doi.org/10.1016/j.jcat.2011.09.034>.
- [32] Y.L. Wan, Q. Guo, K. Wang, X.T. Wang, Efficient and selective photocatalytic oxidation of cyclohexane using O<sub>2</sub> as oxidant in VOCl<sub>2</sub> solution and mechanism insight, *Chem. Eng. Sci.* 203 (2019) 163–172, <https://doi.org/10.1016/j.ces.2019.03.079>.
- [33] W. Wu, Z. Fu, X. Wen, Y. Wang, S. Zou, Y. Meng, Y. Liu, S.R. Kirk, D. Yin, Light-triggered oxy-chlorination of cyclohexane by metal chlorides, *Appl. Catal. A Gen.* 469 (2014) 483–489, <https://doi.org/10.1016/j.apcata.2013.08.045>.
- [34] B. Delley, From molecules to solids with the DMol<sup>3</sup> approach, 7756–42, *J. Chem. Phys.* 113 (2000), <https://doi.org/10.1063/1.1316015>.
- [35] J.P. Perdew, K. Burke, M. Ernzerhof, Generalized gradient approximation made simple, *Phys. Rev. Lett.* 77 (1996) 3865–3868, <https://doi.org/10.1103/PhysRevLett.77.3865>.
- [36] J.P.P. Ramalho, F. Illas, Theoretical study of the adsorption and dissociation of azobenzene on the rutile TiO<sub>2</sub> (110) surface, *Chem. Phys. Lett.* 501 (2011) 379–384, <https://doi.org/10.1016/j.cplett.2010.11.007>.
- [37] W.S. Lee, M.C. Akatay, E.A. Stach, F.H. Ribeiro, W.N. Delgass, Reproducible preparation of Au/TS-1 with high reaction rate for gas phase epoxidation of propylene, *J. Catal.* 287 (2012) 178–189, <https://doi.org/10.1016/j.jcat.2011.12.019>.
- [38] M.R. Morales, B.P. Barbero, L.E. Cadus, Evaluation and characterization of Mn-Cu mixed oxide catalysts for ethanol total oxidation: influence of copper content, *Fuel* 87 (2008) 1177–1186, <https://doi.org/10.1016/j.fuel.2007.07.015>.

- [39] M. Han, B.G. Lee, B.S. Ahn, D.J. Moon, S.I. Hong, Surface properties of CuCl<sub>2</sub>/AC catalysts with various Cu contents: XRD, SEM, TG/DSC and CO-TPD analyses, *Appl. Surf. Sci.* 211 (2003) 76–81, [https://doi.org/10.1016/S0169-4332\(03\)00177-6](https://doi.org/10.1016/S0169-4332(03)00177-6).
- [40] C. Li, G. Xiong, J.K. Liu, P.L. Ying, Q. Xin, Z.C. Feng, Identifying framework titanium in TS-1 zeolite by UV resonance Raman spectroscopy, *J. Phys. Chem. B* 105 (2001) 2993–2997, <https://doi.org/10.1021/jp0042359>.
- [41] W.J. Zhou, R. Wischert, K. Xue, Y.T. Zheng, B. Albela, L. Bonneviot, J.M. Clacens, F.D. Campo, M.P. Titus, P. Wu, Highly selective liquid-phase oxidation of cyclohexane to KA oil over Ti-MWW catalyst: evidence of formation of oxyl radicals, *ACS Catal.* 4 (2014) 53–62, <https://doi.org/10.1021/cs400757j>.
- [42] F.E.O. Medeiros, B.S. Araújo, A.P. Ayala, Raman spectroscopy investigation of the thermal stability of the multiferroic CuCl<sub>2</sub> and its hydrated form, *Vib. Spectrosc.* 99 (2018) 1–6, <https://doi.org/10.1016/j.vibspec.2018.08.006>.
- [43] A.S. Soult, D.F. Carter, H.D. Schreiber, L.J. Burgt, A.E. Stiegman, Spectroscopy of amorphous and crystalline Titania–silica materials, *J. Phys. Chem. B* 106 (2002) 9266–9273, <https://doi.org/10.1021/jp020812c>.
- [44] Y. Hasegawa, A. Ayame, Investigation of oxidation states of titanium in titanium silicalite-1 by X-ray photoelectron spectroscopy, *Catal. Today* 71 (2001) 177–187, [https://doi.org/10.1016/S0920-5861\(01\)00428-X](https://doi.org/10.1016/S0920-5861(01)00428-X).
- [45] C. Xie, Q. Yang, Z. Xu, X. Liu, Y. Du, New route to synthesize highly active nanocrystalline sulfated titania–silica: Synergetic effects between sulfate species and silica in enhancing the photocatalysis efficiency, *J. Phys. Chem. B* 110 (2006) 8587–8592, <https://doi.org/10.1021/jp060266d>.
- [46] J.P. Yang, Y.C. Zhao, J.Y. Zhang, C.G. Zheng, Removal of elemental mercury from flue gas by recyclable CuCl<sub>2</sub> modified magnetospheres catalyst from fly ash. Part 2. Identification of involved reaction mechanism, *Fuel* 167 (2016) 366–374, <https://doi.org/10.1016/j.fuel.2015.11.003>.
- [47] K. Bhattacharyya, S. Varma, A.K. Tripathi, S.R. Bharadwaj, A.K. Tyagi, Effect of vanadia doping and its oxidation state on the photocatalytic activity of TiO<sub>2</sub> for gas-phase oxidation of ethene, *J. Phys. Chem. C* 112 (2008) 19102–19112, <https://doi.org/10.1021/jp807860y>.
- [48] J.M. Valero, S. Obregón, G. Colón, Active site considerations on the photocatalytic H<sub>2</sub> evolution performance of Cu-doped TiO<sub>2</sub> obtained by different doping methods, *ACS Catal.* 4 (2014) 3320–3329, <https://doi.org/10.1021/cs500865y>.
- [49] X. Cai, Y. Xie, S. Wu, Y. Tang, An EPR study on CuCl<sub>2</sub>/γ-Al<sub>2</sub>O<sub>3</sub> catalyst, *Chin. J. Magn. Reson.* 9 (1992) 247–256.
- [50] G. Leofanti, M. Padovan, M. Garilli, D. Carmello, A. Zecchina, G. Spoto, S. Bordiga, G. Turnes Palomino, C. Lamberti, Alumina-supported copper chloride 1. Characterization of freshly prepared catalyst, *J. Catal.* 189 (2000) 91–104, <https://doi.org/10.1006/jcat.1999.2687>.
- [51] A.J. Rouco, TPR study of Al<sub>2</sub>O<sub>3</sub>- and SiO<sub>2</sub>-supported CuCl<sub>2</sub> catalysts, *Appl. Catal. A Gen.* 117 (1994) 139–149, [https://doi.org/10.1016/0926-860X\(94\)85094-1](https://doi.org/10.1016/0926-860X(94)85094-1).
- [52] G.Q. Zou, W.Z. Zhong, Q. Xu, J.F. Xiao, C. Liu, Y.Q. Li, L.Q. Mao, S.R. Kirk, D. L. Yin, Oxidation of cyclohexane to adipic acid catalyzed by Mn-doped titanasilicate with hollow structure, *Catal. Commun.* 58 (2015) 46–52, <https://doi.org/10.1016/j.catcom.2014.08.026>.
- [53] M. Anpo, H. Yamashita, Y. Ichihashi, Y. Fujii, M. Honda, Photocatalytic reduction of CO<sub>2</sub> with H<sub>2</sub>O on titanium oxides anchored within micropores of zeolites: effects of the structure of the active sites and the addition of Pt, *J. Phys. Chem. B* 101 (1997) 2632–2636, <https://doi.org/10.1021/jp962696h>.
- [54] C. Lamberti, S. Bordiga, D. Arduino, A. Zecchina, F. Geobaldo, G. Spano, F. Genoni, G. Petrini, A. Carati, F. Villain, Evidence of the presence of two different framework Ti (IV) species in Ti–silicalite-1 in vacuo conditions: an EXAFS and a photoluminescence study, *J. Phys. Chem. B* 102 (1998) 6382–6390, <https://doi.org/10.1021/jp981225n>.
- [55] F.T. Liang, W.Z. Zhong, L.P. Xiang, L.Q. Mao, Q. Xu, S.R. Kirk, D.L. Yin, Synergistic hydrogen atom transfer with the active role of solvent: preferred one-step aerobic oxidation of cyclohexane to adipic acid by N-hydroxyphthalimide, *J. Catal.* 378 (2019) 256–269, <https://doi.org/10.1016/j.jcat.2019.08.042>.
- [56] J. Kerr, Bond dissociation energies by kinetic methods, *Chem. Rev.* 66 (1966) 465–500, <https://doi.org/10.1021/cr60243a001>.
- [57] H. Gr̈unewald, Handbook of Chemistry and Physics. Von RC Weast. The Chemical Rubber Co., Cleveland, Ohio/USA 1972. 52. Aufl., XXVII, 2313 S., geb. DM 99.80, *Angew. Chem.* 84(1972), 121 445–446, DOI 10.1002/ange.19720840921.
- [58] S. Yashonath, J.M. Thomas, A.K. Nowak, A.K. Cheetham, The siting, energetics and mobility of saturated hydrocarbons inside zeolitic cages: methane in zeolite Y, *Nature* 331 (1988) 601–604, <https://doi.org/10.1038/331601a0>.
- [59] R. Chen, C.J. Yang, Q.Q. Zhang, B.G. Zhang, K.J. Deng, Visible-light-driven selective oxidation of glucose in water with H-ZSM-5 zeolite supported biomimetic photocatalyst, *J. Catal.* 374 (2019) 297–305, <https://doi.org/10.1016/j.jcat.2019.04.044>.
- [60] H.M. Wang, W.Y. Shi, Y.L. Li, M.M. Yu, Y. Gao, A.W. Lei, Photoinduced radical relay way toward α-CF<sub>3</sub> ketones with low-cost trifluoromethylation reagents, *CCS Chem.* 2 (2020) 1710–1712, <https://doi.org/10.31635/ccschem.020.202000386>.
- [61] M. Somekh, A.M. Khenkin, A. Herman, R. Neumann, Selective visible light aerobic photocatalytic oxygenation of alkanes to the corresponding carbonyl compounds, *ACS Catal.* 9 (2019) 8819–8824, <https://doi.org/10.1021/acscatal.9b02999>.
- [62] N.J. Turro, Supramolecular photochemistry. A paradigm for the 1990s, *J. Photochem. Photobiol. A-Chem.* 100 (1996) 53–56, [https://doi.org/10.1016/S1010-6030\(96\)04444-9](https://doi.org/10.1016/S1010-6030(96)04444-9).